



© Copyright by  
Sanbir S. Kaler 2014  
All Rights Reserved

**Etching of Si and SiN<sub>x</sub> by Beams Emanating from Inductively Coupled  
CH<sub>3</sub>F/O<sub>2</sub> and CH<sub>3</sub>F/CO<sub>2</sub> Plasmas**

A Thesis

Presented to the Faculty of  
the Department of Chemical & Biomolecular Engineering  
University of Houston

In Partial Fulfillment  
Of the Requirements for the Degree  
Master of Science  
In Chemical Engineering

by

Sanbir S. Kaler

August 2014

**Etching of Si and SiN<sub>x</sub> by Beams Emanating from Inductively Coupled  
CH<sub>3</sub>F/O<sub>2</sub> and CH<sub>3</sub>F/CO<sub>2</sub> Plasmas**

---

Sanbir S. Kaler

Approved:

---

Co-Chair of the Committee  
Vincent M. Donnelly, Ph.D  
Chemical and Biomolecular Engineering  
Professor

---

Co-Chair of the Committee  
Demetre J. Economou, Ph.D  
Chemical and Biomolecular Engineering  
Professor

Committee Members:

---

Gila Stein, Ph.D  
Chemical and Biomolecular Engineering  
Assistant Professor

---

Paul Ruchhoeft, Ph.D  
Electrical and Computer Engineering  
Associate Professor

---

Suresh K. Khator, Ph.D  
Cullen College of Engineering  
Associate Dean

---

Michael P. Harold, Ph.D  
Chemical and Biomolecular Engineering  
Professor and Department Chairman

**Etching of Si and SiN<sub>x</sub> by Beams Emanating from Inductively Coupled  
CH<sub>3</sub>F/O<sub>2</sub> and CH<sub>3</sub>F/CO<sub>2</sub> Plasmas**

An Abstract

Of a

Thesis

Presented to

the Faculty of the Department of Chemical & Biomolecular Engineering

University of Houston

In Partial Fulfillment

Of the Requirement for the Degree

Master of Science

in Chemical Engineering

by

Sanbir S. Kaler

August 2014

## Abstract

In advanced microelectronic device fabrications, novel gate electrode designs for field effect transistors (FinFETs) require highly anisotropic and selective silicon nitride ( $\text{SiN}_x$ ) etching over Si and/or  $\text{SiO}_2$ .  $\text{SiN}_x$  substrates and p-Si on Ge substrates were etched with  $\text{CH}_3\text{F}/\text{O}_2$  and  $\text{CH}_3\text{F}/\text{CO}_2$  inductively coupled plasma beams. In addition, polymer films deposited on p-Si and  $\text{SiN}_x$  were characterized and compared via x-ray photoelectron spectroscopy analyses. Optical emission species intensity and species number density of the hydro-fluorocarbon plasma, as a function of %  $\text{O}_2$  and  $\text{CO}_2$  addition were compared. Etch and deposition rates were measured on either side of abrupt transitions in gas-phase species concentration, detected at  $\sim 48\%$   $\text{O}_2$  and  $\sim 74\%$   $\text{CO}_2$ . These transition point compositions correspond to a switch from polymer-coated to polymer-free reactor walls.

*Keywords:* Silicon-nitride etching, Hydro-fluorocarbon plasmas

# Table of Contents

Abstract .....	vi
Table of Contents .....	vii
List of Figures .....	viii
Chapter 1 Introduction .....	1
1.1 Plasma Etching .....	1
1.2 Capacitive and Inductive RF discharges .....	1
1.3 The Importance of Silicon Nitride .....	2
1.4 Challenges .....	3
1.5 Statement of Purpose .....	3
Chapter 2 Literature Review .....	4
2.1 Etching .....	4
2.2 CF <sub>4</sub> /O <sub>2</sub> Plasmas and Etching of Si and SiO <sub>2</sub> .....	4
2.3 Etching of SiN <sub>x</sub> in 'Free' F Atom and Fluorocarbon Radical Containing Plasmas .....	10
2.4 Selective Etching of Silicon Nitride using Hydro-Fluorocarbon Plasmas .....	10
2.5 Polymer Films on SiN <sub>x</sub> after Etching with Hydro-Fluorocarbon Plasma .....	16
Chapter 3 Experimental .....	20
3.1 Apparatus .....	20
3.2 X-Ray Photoelectron Spectroscopy .....	22
3.3 Optical Emission Spectroscopy .....	24
3.4 Mass Spectrometer .....	24
3.5 Spectroscopic Ellipsometry .....	24
Chapter 4 Results and Discussions .....	25
4.1 Selected Optical Emission Measurements .....	25
4.2 Deposition of Polymer on Si with CH <sub>3</sub> F/O <sub>2</sub> and CH <sub>3</sub> F/CO <sub>2</sub> Plasma .....	29
4.3 Etched Si on Ge with CH <sub>3</sub> F/O <sub>2</sub> and CH <sub>3</sub> F/CO <sub>2</sub> Plasmas .....	35
4.4 Deposition of Polymer Film on SiN <sub>x</sub> .....	42
4.5 SiN <sub>x</sub> Etching with CH <sub>3</sub> F/O <sub>2</sub> and CH <sub>3</sub> F/CO <sub>2</sub> Plasmas .....	46
Chapter 5 Summary and Conclusions .....	50
References .....	51

## List of Figures

Fig. 1	F atom concentration in $\text{CF}_4/\text{O}_2$ plasma of the feed determined by gas-phase titration <sup>11</sup> .....	5
Fig. 2	Comparison of results via computer simulations of $\text{CF}_4/\text{O}_2$ plasmas with that of Smolinsky and Flamm's experimental data <sup>13</sup> .....	6
Fig. 3	Normalized etch rate of Si and F emission from $\text{CF}_4/\text{O}_2$ plasma <sup>11</sup> .....	8
Fig. 4	Relative etch rates of Si and $\text{SiO}_2$ (solid lines, points) as well as relative F atom concentration (dashed lines) <sup>14</sup> .....	9
Fig. 5	$\text{SiN}_x$ etch rate and F radical emission intensity are shown at $\text{C}_4\text{F}_8$ (10 sccm) + Ar (150 sccm) with added feed gas $\text{CH}_3\text{F}$ , $\text{CH}_2\text{F}_2$ , and $\text{CHF}_3$ <sup>31</sup> .....	11
Fig. 6	$\text{SiO}_2$ and $\text{SiN}_x$ etch rates vs. added $\text{H}_2$ in $\text{C}_4\text{F}_8$ + Ar plasma <sup>31</sup> .....	12
Fig. 7	$\text{Si}_3\text{N}_4$ and $\text{SiO}_2$ etch rates versus $\text{O}_2$ % increase in fluorocarbon gases <sup>32</sup> .....	13
Fig. 8	Normalized optical emission intensities for Ar (750.4 nm), F (703.4 nm), CF (240nm), $\text{CF}_2$ (252 nm) and H (656.5 nm) versus $\text{O}_2$ % increase in fluorocarbon gases <sup>32</sup> .....	14
Fig. 9	Normalized H emission intensity and $\text{Si}_3\text{N}_4$ etch rate versus $\text{O}_2$ % increase in fluorocarbon gases <sup>32</sup> .....	15
Fig. 10	Polymer thickness formed on etched surfaces in hydro-fluorocarbon plasma <sup>32</sup> .....	16
Fig. 11	XPS spectra after etching $\text{Si}_3\text{N}_4$ and $\text{SiO}_2$ with $\text{CH}_3\text{F}/\text{O}_2$ plasma <sup>32</sup> .....	17
Fig. 12	$\text{Si}_3\text{N}_4$ etch rate and hydro-fluorocarbon film thickness versus $\text{H}_2$ flow rate addition to $\text{CH}_2\text{F}_2$ + Ar <sup>33</sup> .....	18
Fig. 13	Etch rates of $\text{SiO}_2$ , $\text{Si}_3\text{N}_4$ , SiCH, and Si in multiple fluorocarbon plasmas as a function of self-biased voltage. $\text{CF}_x$ film thicknesses were measured <sup>35</sup> .....	18
Fig. 14	Schematic of compact, inductively coupled plasma source. ....	20
Fig. 15	Top view schematic of the overall system consisting of a plasma chamber, load lock chamber, ICP plasma reactor, mass spectrometer, and XPS.....	21
Fig. 16	Normalized number densities for $(n\text{H}/n\text{Ar})/80.36$ , $(n\text{F}/n\text{Ar})/2.89$ and $(n\text{O}/n\text{Ar})/24.58$ , and normalized intensity ratios for $\text{HF}^+/\text{Ar}$ , as a function of $\text{CO}_2$ or $\text{O}_2$ addition <sup>42</sup> .....	25
Fig. 17	Normalized intensity ratios of $\text{CH}/\text{Xe}$ , $\text{CF}/\text{Xe}$ , $\text{C}/\text{Xe}$ , and $\text{OH}/\text{Xe}$ emission as function of $\text{CO}_2$ or $\text{O}_2$ addition <sup>42</sup> .....	26

Fig. 18 Normalized number densities for $(n_{\text{CO}}/n_{\text{Xe}})/84.35$ and $(n_{\text{CO}_2^+}/n_{\text{Ar}})/27.59$ as a function of $\text{CO}_2$ or $\text{O}_2$ addition <sup>42</sup> .....	27
Fig. 19 Mass spectrometry spectra displays nearly complete dissociation of $\text{CH}_3\text{F}$ into stable products. ....	28
Fig. 20 Film deposition rates on p-Si for $\text{CH}_3\text{F}/\text{O}_2$ and $\text{CH}_3\text{F}/\text{CO}_2$ plasmas at 300 W, 10 mTorr, and no boundary bias <sup>42</sup> .....	29
Fig. 21 The C (1s) spectra of deposited film on p-Si as a function of a.) $\text{CH}_3\text{F}/\text{O}_2$ and b.) $\text{CH}_3\text{F}/\text{CO}_2$ plasma <sup>42</sup> .....	31
Fig. 22 The Si (2p) spectra of deposited film on p-Si as a function of a.) $\text{CH}_3\text{F}/\text{O}_2$ and b.) $\text{CH}_3\text{F}/\text{CO}_2$ plasma <sup>42</sup> .....	32
Fig. 23 The O (1s) spectra of deposited film on p-Si as a function of a.) $\text{CH}_3\text{F}/\text{O}_2$ and b.) $\text{CH}_3\text{F}/\text{CO}_2$ plasma <sup>42</sup> .....	33
Fig. 24 The F (1s) spectra of deposited film on p-Si as a function of a.) $\text{CH}_3\text{F}/\text{O}_2$ and b.) $\text{CH}_3\text{F}/\text{CO}_2$ plasma <sup>42</sup> .....	34
Fig. 25 Relative abundance of species at thermodynamic equilibrium in $\text{CH}_3\text{F}/\text{O}_2$ (hole symbol) and $\text{CH}_3\text{F}/\text{CO}_2$ (solid symbol) plasmas at 10 mTorr and a temperature of 373 K. Overlapping plots convey no difference in trends <sup>42</sup> .....	35
Fig. 26 Si thickness remaining on Ge after exposing to $\text{CH}_3\text{F}/\text{O}_2$ (solid circles) and $\text{CH}_3\text{F}/\text{CO}_2$ (open circles) plasmas at 300 W and 10 mTorr without boundary .....	36
Fig. 27 Ge (3d) XPS spectrum of Si on Ge without HF dip. ....	37
Fig. 28 Si (2p) XPS spectrum of Si on Ge without HF.....	38
Fig. 29 XPS spectra of Si on Ge after exposing wafer to $\text{CH}_3\text{F}/\text{O}_2$ (a.) and $\text{CH}_3\text{F}/\text{CO}_2$ (b.) focused on Si (2p) region. Si (2p) peaks were normalized to unity at plasma conditions 300 W and 10 mTorr. ....	39
Fig. 30 XPS spectra of Si on Ge after exposing wafer to $\text{CH}_3\text{F}/\text{O}_2$ (a.) and $\text{CH}_3\text{F}/\text{CO}_2$ (b.) focused on Ge (3d) region. Ge (3d) peaks were normalized to unity at plasma conditions 300 W and 10 mTorr. ....	41
Fig. 31 Polymer film deposition on $\text{SiN}_x$ as function of $\text{O}_2\%$ addition rates. $\text{CH}_3\text{F}/\text{O}_2$ power and pressure was 300 W and 10 mTorr, respectively. ....	43
Fig. 32 XPS spectra of polymer film deposited on $\text{SiN}_x$ comprising of a) C (1s), b) Si	

(2p), c) O (1s) d) F(1s), and e) N(1s) peaks.....	46
Fig. 33 SiN <sub>x</sub> thickness change was measured using an ellipsometry after exposing the substrate to CH <sub>3</sub> F 20% O <sub>2</sub> 80% plasma beam at a constant flow rate of 10 sccm. Plasma was maintained at 300 W and 10 mTorr without boundary bias.....	47
Fig. 34 SiN <sub>x</sub> thickness change was measured using an ellipsometry after exposing the substrate to CH <sub>3</sub> F 20% CO <sub>2</sub> 80% plasma beam at a constant flow rate of 10 sccm. Plasma was maintained at 300 W and 10 mTorr without boundary bias.....	47
Fig. 35 SiN <sub>x</sub> etch rates measured using a spectroscopic ellipsometry as a function of O <sub>2</sub> % and CO <sub>2</sub> % addition. The plasma power was 300 W and pressure was 10 mTorr. ....	49

# Chapter 1 Introduction

## 1.1 Plasma Etching

Integrated circuitry functionality has improved dramatically over the past 40 years. This is reflected in Moore's law, which notes the number of transistors on integrated circuits has doubled every two and a half years during this period<sup>1</sup>. The smallest feature size for the first commercially available microprocessor in 1971 (Intel 4004) was  $10\ \mu\text{m}^2$ . In September of 2013, Intel announced feature size available 3D Si Fin field-effect transistors (FETS), or "FinFETs" with 22 nm fin widths<sup>3</sup>. They project these dimensions will shrink to 10 nm sized IC as early as 2015<sup>3</sup>.

Spawned by the need to reduce toxic waste in wet etching processes and requirement for improved resolution in pattern transfer, plasma etching emerged in the 1970s as a critical process in integrated circuit manufacturing<sup>4</sup>. Along with the phenomenal advances in optical lithography, the remarkable improvements in plasma processing of semiconductor materials have allowed the advancement of this industry to continue unabated. Plasma etching is used to transfer lithographically defined patterns in photoresist material to one material while leaving exposed any underlying materials intact. This selectivity is a key component of plasma etching, along with anisotropy, vertical etching rates with minimal horizontal etching<sup>5</sup>. These unique features and the ability to transfer integrated circuit patterns of incredibly small feature sizes has prompted the study of plasma processing and its reaction mechanisms and kinetics.

## 1.2 Capacitive and Inductive RF discharges

Etching, early on, was primarily done using dual-frequency capacitively-coupled plasma reactors (CCP)<sup>4</sup>. A high rf frequency above 13.56 MHz is typically applied the

smaller of two parallel electrodes. Due to the asymmetrical structure of electrodes, a negative dc self-bias voltage was placed on the smaller electrode causing more energetic ion bombardment of substrates/anisotropic etching. More recently, dual frequency CCP reactors have been developed, with high frequency (typically 13.56 to 50 MHz) applied to an upper electrode, and a lower frequency applied to the lower electrode (usually lower than 13.56 MHz) to generate high-voltage sheaths on the lower electrode that holds the wafer. These are considered low-density discharges that lead to stochastic heating in the plasma sheath region (no collisions). High-density discharges are produced from microwave or rf driven inductively coupled plasmas (ICP) which contain low-voltage sheaths near the whole surface. ICP reactors deliver rf power to the plasma through a dielectric window, tube, or dome. This allows for better ion energy control due to the ability to separately provide energy to the separately rf-powered electrode on which the substrate sits. Much higher etching rates and much higher selectivities were achieved with ICP etchers, making them the tools of choice for etching gate-electrodes and for  $\text{SiN}_x$  etching required for FinFET.

### **1.3 The Importance of Silicon Nitride**

Silicon nitride is used as a hard mask/gate spacer material in many complex feature size applications. It is often applied as a spacer on the sides of gates in FETs to tune channel length and transistor properties.<sup>4</sup>  $\text{SiN}_x$  creates a physical barrier that is superior to  $\text{SiO}_2$  for penetration by water vapor, salts, and other species<sup>5</sup>. Furthermore,  $\text{SiN}_x$  is effective in preventing oxygen from reaching and oxidizing the underlying layer (e.g. Si), as well as preventing Si damage or loss relative to  $\text{SiO}_2$  gate spacers. Si damage

or loss would lead to source/drain shorts, causing substrate bias dependent leakage in FETs.<sup>4</sup>

#### **1.4 Challenges**

The challenge, however, in SiN<sub>x</sub> etching is to maintain a high selectivity over etching of Si and SiO<sub>2</sub>. High F-atom generating plasma feed gases, such as CF<sub>4</sub>/O<sub>2</sub> or NF<sub>3</sub>/O<sub>2</sub>, provide etch rates of 30 nm/min SiN<sub>x</sub><sup>9</sup>. This method is not selective with respect to silicon. Anisotropic etching with high selectivity over Si and moderate selectivity over SiO<sub>2</sub> is achieved through ion bombardment using fluorocarbon gases with equivalent C to F atom ratio, such as CH<sub>3</sub>F<sup>15</sup>. Previous studies are examined in the ‘literature review’.

#### **1.5 Statement of Purpose**

Despite its importance for highly selective etching of SiN<sub>x</sub> on Si or SiO<sub>2</sub> for present and future integrated circuit manufacturing, the fundamental mechanisms for SiN<sub>x</sub> etching in hydro-fluorocarbon feed gas plasmas has not been reported. Thus, the purpose of this study is to carry out experiments examining inductively coupled plasmas with CH<sub>3</sub>F/O<sub>2</sub> and CH<sub>3</sub>F/CO<sub>2</sub> feed gas while etching SiN<sub>x</sub> and Si. Particular focus on the hydro-fluorocarbon films that deposit during etching.

# Chapter 2 Literature Review

## 2.1 Etching

Plasma etching (also frequently referred to as reactive ion etching, RIE) involves a combination of neutral species chemical reactions on the surface, influenced by positive ion bombardment. The choice of etchant is determined by many factors including material or substrate type, anisotropy, selectivity, loading, and texture<sup>10</sup>. Isotropic etching occurs when chemical ‘gasification’ reactions between etchant species and a substrate occur with little or no influence by ion bombardment<sup>10</sup>. An undercut circular wall profile is produced at the mask edge, where the radius length is equal to the etch depth<sup>11</sup>. Vertical sidewalls on etched lines and trenches require the ion flux to be perpendicular to substrate surface to stimulate etching reactions that occur at the bottoms of features at a rate that is much faster than on side walls<sup>10</sup>. Additional species may be required to suppress chemical etching on the side walls to prevent isotropic etching. Anisotropic etching is required when trying to create nano-features with high aspect ratios (deep via holes or capacitor trenches)<sup>10</sup>.

Atomic fluorine reacts rapidly with all types of Si, SiO<sub>2</sub>, and silicon nitride (SiN<sub>x</sub>) forming stable, volatile products<sup>21</sup>. It is well understood that fluorocarbon radicals also promote etching of these materials<sup>12</sup>. Though fluorocarbon-containing plasmas are commonly used in industry, and have been studied extensively for etching of Si and SiO<sub>2</sub>, mechanisms for etching SiN have not been reported.

## 2.2 CF<sub>4</sub>/O<sub>2</sub> Plasmas and Etching of Si and SiO<sub>2</sub>

Mogab, et al. showed that oxygen addition in fluorocarbon plasma increased atomic fluorine concentration, in figure 1<sup>11</sup>.

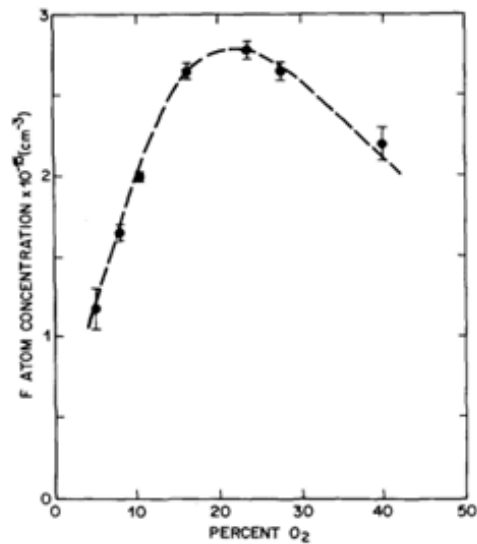
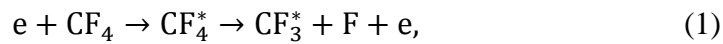
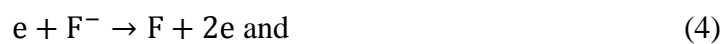


Fig. 1 F atom concentration in CF<sub>4</sub>/O<sub>2</sub> plasma of the feed determined by gas-phase titration<sup>11</sup>.

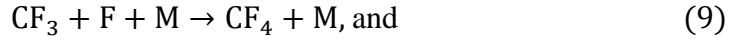
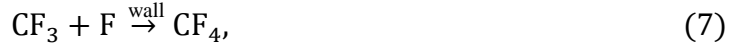
F atom concentration eventually reached a maximum at 22% O<sub>2</sub> and then decreased as O<sub>2</sub> further diluted the feed gas, CF<sub>4</sub>. They also proposed a model, summarized briefly below. Electron-impact dissociation of CF<sub>4</sub> molecules yielded F, negative ions F<sup>-</sup> and radicals CF<sub>3</sub><sup>\*11</sup> listed as



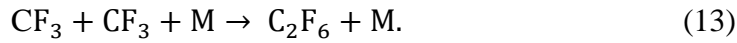
F<sup>-</sup> and CF<sub>3</sub><sup>\*</sup> undergo a detachment reaction and dissociative recombination, respectively, to create additional atomic fluorine<sup>11</sup> shown as



F, F<sup>-</sup>, and CF<sub>3</sub> are lost by heterogeneous, homogeneous, and third body recombination reactions forming stable F<sub>2</sub> and CF<sub>4</sub><sup>11</sup> written as



A small amount of C<sub>2</sub>F<sub>6</sub><sup>11</sup> was also formed in their proposed model shown as



With the addition of oxygen, production of stable CO, CO<sub>2</sub>, and COF<sub>2</sub> species are detected downstream with simultaneous reduction in fluorocarbon.

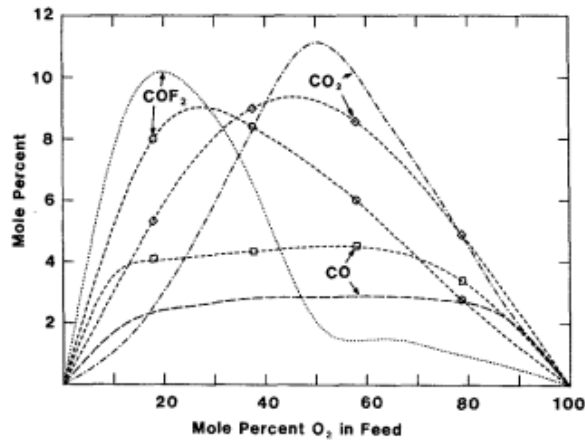
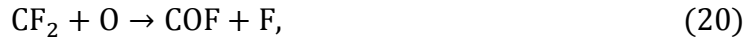
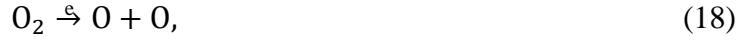


Fig. 2 Comparison of results via computer simulations of CF<sub>4</sub>/O<sub>2</sub> plasmas with that of Smolinsky and Flamm's experimental data<sup>13</sup>.

Extensive computer model simulations of CF<sub>4</sub>/O<sub>2</sub> plasma were carried out by Plumb and Ryan<sup>13</sup>. Their simulations incorporated 13 of their listed 49 reactions<sup>13</sup>





Their model predictions (reproduced in figure 2, lines without symbols) were compared with experimental data of Smolinsky and Flamms (lines with symbols in figure 2). The model was in reasonable agreement with reactions which produce CO, COF<sub>2</sub>, and CO<sub>2</sub> number density with the addition of oxygen to the plasma. Small discrepancies were ascribed to the difference in experimental and calculated rate coefficients for the dissociative reactions<sup>13</sup>. Major significance was given to reaction equation (19) which confirms an increase in fluorine atom concentration with the addition of O<sub>2</sub>. The curvature in figure 2 of fluorine atom concentration was similar to that of COF<sub>2</sub> with both maximums observed around 22%. The simulations however, disagreed with experiments in the atomic fluorine number density<sup>13</sup>. The ratio of F<sub>2</sub>/F changed throughout O<sub>2</sub> percent addition in the simulations whereas it did not change the experimental work of Flamm et

al.<sup>13</sup>. This was partly attributed to the differences in the reactor model (designed in simulation) and actual experimental reactor used by Flamm et al.. Differences in dissociative reaction rate coefficients can also be attributed to the disagreement in F atom number density<sup>13</sup>.

Mogab et al.<sup>11</sup> and d'Agostino et al.<sup>14</sup> conducted analogous experiments found similar behavior of Si and SiO<sub>2</sub> etch rates and atomic fluorine density with addition of % O<sub>2</sub>. Both results are shown in figures 3 and 4.

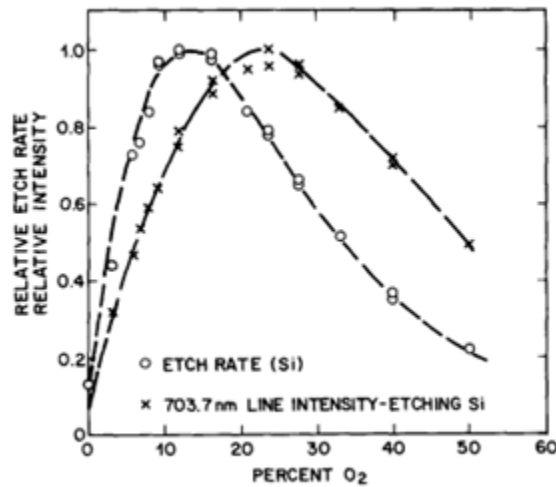


Fig. 3 Normalized etch rate of Si and F emission from CF<sub>4</sub>/O<sub>2</sub> plasma<sup>11</sup>.

The 703.7 nm excited F atom emission intensity and Si etch rate were normalized and plotted versus O<sub>2</sub> addition<sup>11</sup>. Their model states the Si etch rate is not “*strictly*” proportional to the F-atom concentration due to the competition between F etchant atoms and O atoms adsorbing on active Si surface sites<sup>11</sup>. This does not occur in SiO<sub>2</sub> for Si active sites or ‘dangling bonds’ are already filled by O atoms. It was concluded that oxygen percentage addition in CF<sub>4</sub> increased Si etch rate, led to a maximum, and then decreased because of eventual oxidation of Si. Without sample bias or boundary

electrode bias, etching of Si was perceived to be isotropic, non-ion induced etching<sup>15</sup>. When ions are accelerated to the sample, anisotropic etching (ion-enhanced  $\text{CF}_x$ -silicon or  $\text{CF}_3^+$ - reactive ion etching) with slight undercutting was noticed<sup>12</sup>.

D'Agostino et al. had discovered similar results with slight differences in plasma conditions. Referencing figure 4, both Si and  $\text{SiO}_2$  etch rates decreased as O atoms adsorb on active sites<sup>14</sup>.

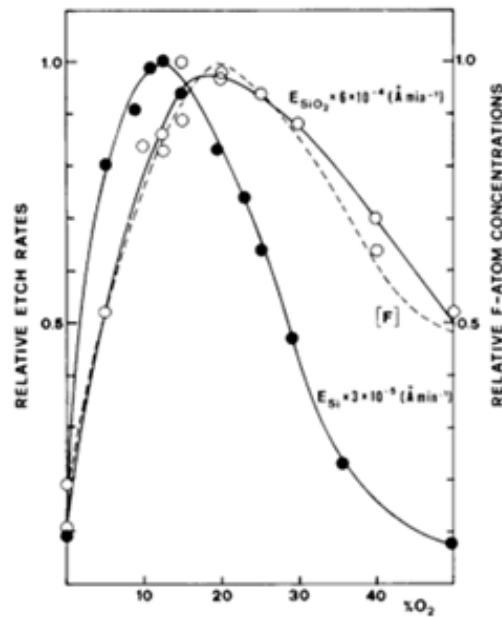


Fig. 4 Relative etch rates of Si and  $\text{SiO}_2$  (solid lines, points) as well as relative F atom concentration (dashed lines)<sup>14</sup>.

The etch rates for Si were about 20 times higher than  $\text{SiO}_2$ . Furthermore, both sets of experiments illustrate the maximum etch rate for Si was ~12 %  $\text{O}_2$  addition, whereas F atom concentration and  $\text{SiO}_2$  maximum etch rate were detected closer to the 22 %  $\text{O}_2$  addition<sup>12</sup>. High selectivity and anisotropy for etching  $\text{SiO}_2$ , however, is achieved using fluorocarbon radicals as primary etchants rather than only F-atom etchants<sup>16-18,39</sup>. Reaction rates for fluorine atoms etching Si and  $\text{SiO}_2$  as a function of temperature and F atom concentration<sup>19</sup> are given by

$$R_{F(\text{Si})} = 2.91 \pm .20 \times 10^{-12} T^{\frac{1}{2}} n_F e^{-\frac{.108}{kT}} \left( \frac{\text{\AA}}{\text{min}} \right) \text{ and } (27)$$

$$R_{F(\text{SiO}_2)} = 6.14 \pm .50 \times 10^{-13} T^{\frac{1}{2}} n_F e^{-\frac{.163}{kT}} \left( \frac{\text{\AA}}{\text{min}} \right). (28)$$

### 2.3 Etching of SiN<sub>x</sub> in ‘Free’ F Atom and Fluorocarbon Radical – Containing Plasmas

SiN<sub>x</sub> can be etched in plasmas that contain large concentrations of F atoms (e.g. CF<sub>4</sub>/O<sub>2</sub><sup>34</sup>), as well as plasmas that contain large concentrations of fluorocarbon radicals (e.g. CHF<sub>3</sub>/O<sub>2</sub><sup>31</sup>). Most plasma that etch SiN will also etch Si and/or SiO<sub>2</sub>. Etching of SiN<sub>x</sub> in CF<sub>4</sub>/O<sub>2</sub> and other ‘F atom containing plasmas results in little to no selectivity (SiN<sub>x</sub>:Si = 1:8)<sup>22</sup>. Very high selectivity of SiN<sub>x</sub> with respect to Si is typically required for CMOS devices, thus making it vital to avoid the use of gases which produce large amounts of F atoms<sup>30</sup>.

### 2.4 Selective Etching of Silicon Nitride using Hydro-Fluorocarbon Plasmas

A highly selective process can be obtained was discovered in rich CHF<sub>x</sub>, CF<sub>x</sub>-rich plasmas, with hydro-fluorocarbon and/or fluorocarbon-containing plasmas. Conditions for fast SiN<sub>x</sub> etching rates were found to be at low pressure, with energetic ion bombardment where SiN<sub>x</sub>:Si etching selectivity ranging from 30 – 100:1<sup>21,23,24,25,26,27,28,29</sup>.

Iijima et al.<sup>31</sup> reported the etching of blanket SiN<sub>x</sub> and SiN<sub>x</sub>/SiO<sub>2</sub> via in inductively coupled plasmas of C<sub>4</sub>F<sub>8</sub> + Ar with added CHF<sub>3</sub>, CH<sub>2</sub>F<sub>2</sub>, and CH<sub>3</sub>F. As shown in figure 5, the SiN<sub>x</sub> etch rate and F optical emission intensity both increased when CHF<sub>3</sub> was added to the plasma, and decreased with CH<sub>3</sub>F addition, suggesting that F atoms are the etchant of SiN<sub>x</sub><sup>31</sup>.

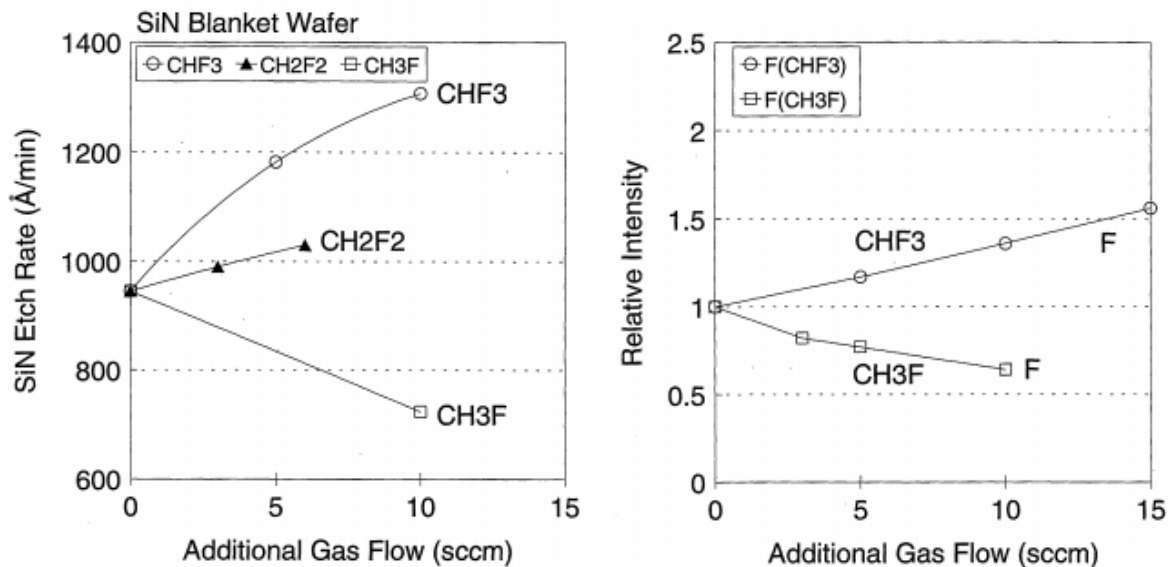


Fig. 5 SiN<sub>x</sub> etch rate and F radical emission intensity are shown at C<sub>4</sub>F<sub>8</sub> (10 sccm) + Ar (150 sccm) with added feed gas CH<sub>3</sub>F, CH<sub>2</sub>F<sub>2</sub>, and CHF<sub>3</sub><sup>31</sup>.

Iijima et al. initially attributed the decrease in etching rate upon CH<sub>3</sub>F addition to the increase in H atom concentration, which results in an increase in depletion of F atoms via formation of HF. When H<sub>2</sub> was added to C<sub>4</sub>F<sub>8</sub> + Ar, however, the etching rate of SiN<sub>x</sub> actually *increased* as shown in figure 6<sup>31</sup>. If the 'F scavenging effect' by H atoms was the explanation of the reduction in etching rate with CH<sub>3</sub>F addition, then the addition of H<sub>2</sub> would be expected to reduce the SiN<sub>x</sub> etch rate even more so than CH<sub>3</sub>F addition<sup>31</sup>. Iijima et al. ascribed the reduction in SiN<sub>x</sub> etching rate with CH<sub>3</sub>F addition to the enhanced role of C-H<sub>x</sub> radicals relative to H atoms for scavenging F through HF formation<sup>31</sup>.

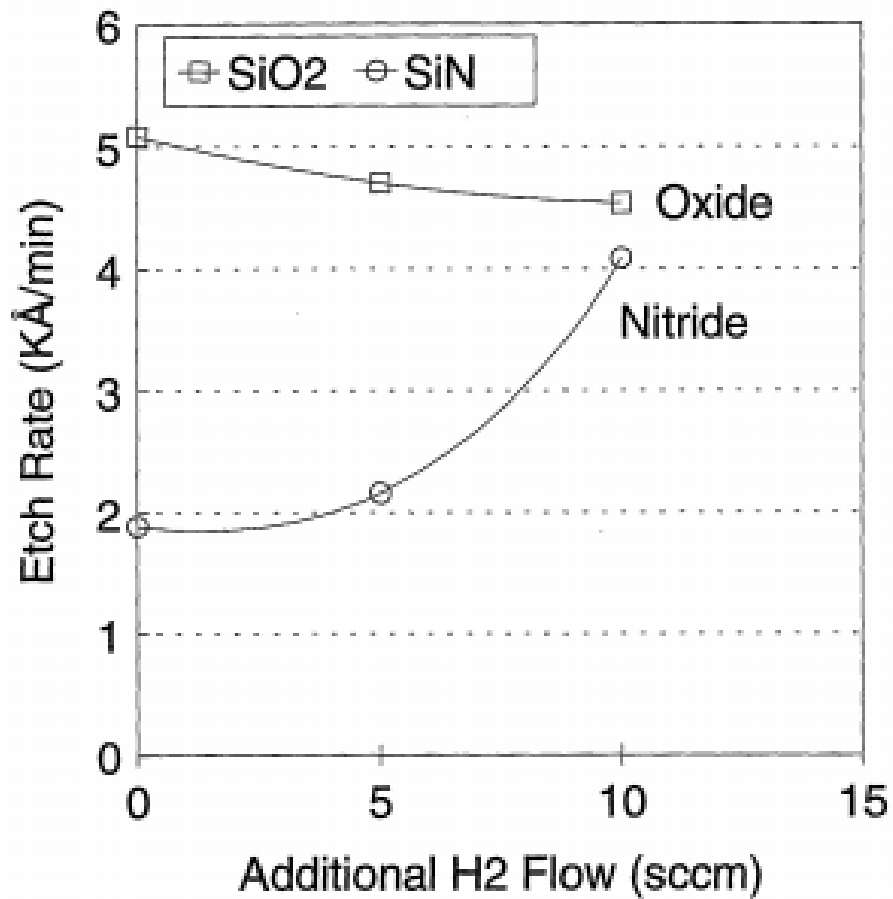


Fig. 6 SiO<sub>2</sub> and SiN<sub>x</sub> etch rates vs. added H<sub>2</sub> in C<sub>4</sub>F<sub>8</sub> + Ar plasma<sup>31</sup>.

Chen et al.<sup>32</sup> reported on the mechanisms of selectively etching Si<sub>3</sub>N<sub>4</sub> over SiO<sub>2</sub> in hydro-fluorocarbon, capacitively-coupled plasmas using CHF<sub>3</sub>, CH<sub>2</sub>F<sub>2</sub>, and CH<sub>3</sub>F with added O<sub>2</sub>. Figure 7 shows etch rates as a function of O<sub>2</sub> addition for constant hydro-fluorocarbon feed<sup>32</sup>. Maximum etch rates were found at 40%, 60%, and 80% O<sub>2</sub> for CHF<sub>3</sub>, CH<sub>2</sub>F<sub>2</sub>, and CH<sub>3</sub>F, respectively. The highest etch rates measured were for CHF<sub>3</sub>, followed by CH<sub>2</sub>F<sub>2</sub> and CH<sub>3</sub>F, consistent with Iijima et al. findings<sup>32</sup>. The authors attributed the reduction of Si<sub>3</sub>N<sub>4</sub> etch rates to the increase in C/F ratio, since F is the main etchant of Si<sub>3</sub>N<sub>4</sub><sup>32</sup>.

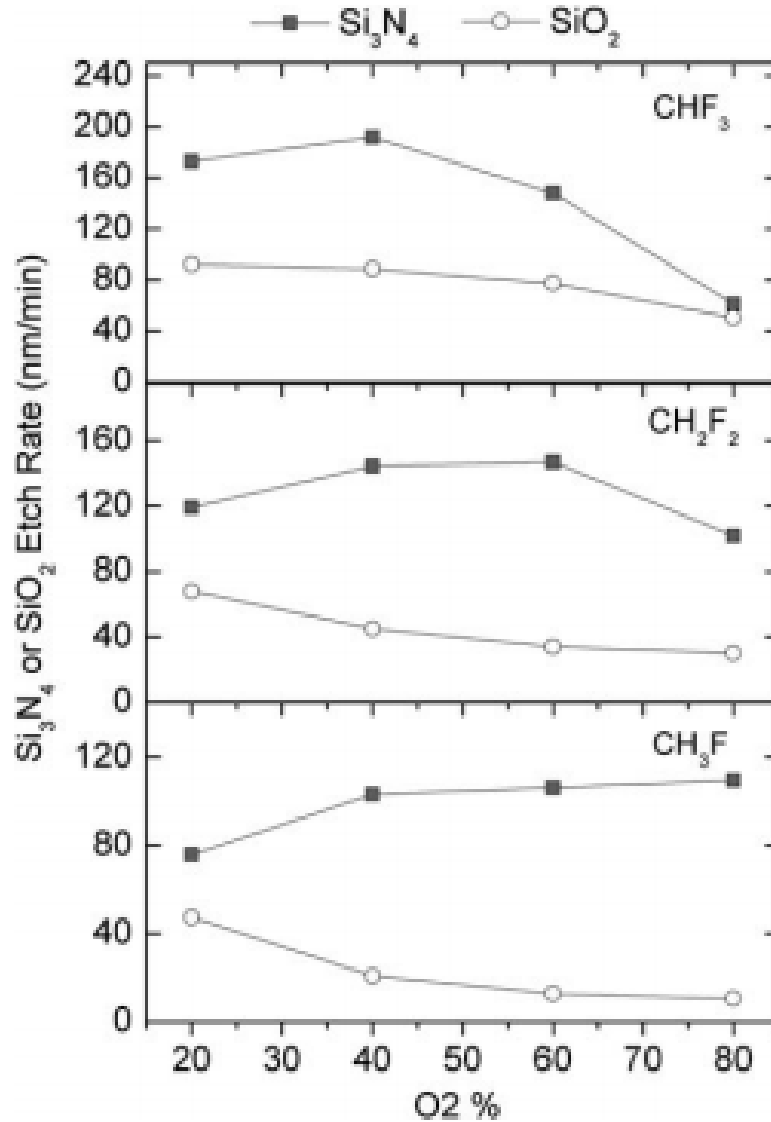


Fig. 7 Si<sub>3</sub>N<sub>4</sub> and SiO<sub>2</sub> etch rates versus O<sub>2</sub> % increase in fluorocarbon gases<sup>32</sup>.

It was also apparent that Si<sub>3</sub>N<sub>4</sub> etch rates decreased as O<sub>2</sub>% increased, as expected (O<sub>2</sub> dilution). This effect was not noticed for CH<sub>3</sub>F at the higher O<sub>2</sub> % region. Referencing figure 8, the normalized optical emission intensity plot versus O<sub>2</sub> % increase, H (656.5 nm) emission intensity initially increased for all hydro-fluorocarbon gases. The initial increase in H emission with added O<sub>2</sub> in hydro-fluorocarbon can be described by



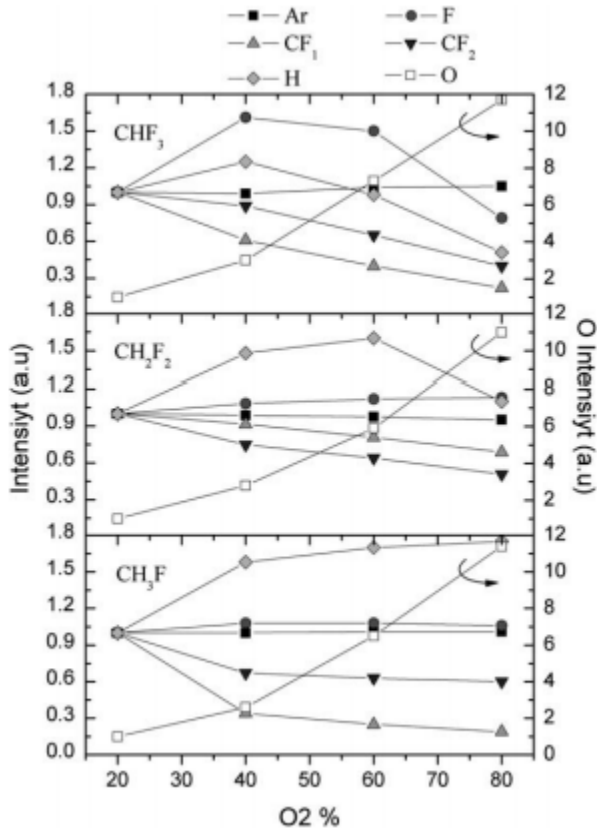


Fig. 8 Normalized optical emission intensities for Ar (750.4 nm), F (703.4 nm), CF (240 nm), CF<sub>2</sub> (252 nm) and H (656.5 nm) versus O<sub>2</sub> % increase in fluorocarbon gases<sup>32</sup>.

A maximum and steady decrease in H atom emission was noticed for both CHF<sub>3</sub> and CH<sub>2</sub>F<sub>2</sub> but not CH<sub>3</sub>F – possibly due to the larger amount of H atoms in methyl fluoride. The authors had discovered a correlation amongst H atoms and Si<sub>3</sub>N<sub>4</sub> etch rate shown by figure 9.

Chen et al. had claimed H atoms play a vital role in the removal of CN - an involatile product within the thin polymer layer on the substrate surface<sup>32</sup>. With large amounts of H in plasma, H radicals diffuse through the polymer layer forming and removing stable HCN. The removal of N atoms from Si<sub>3</sub>N<sub>4</sub> substrate is described by (30) – (32).

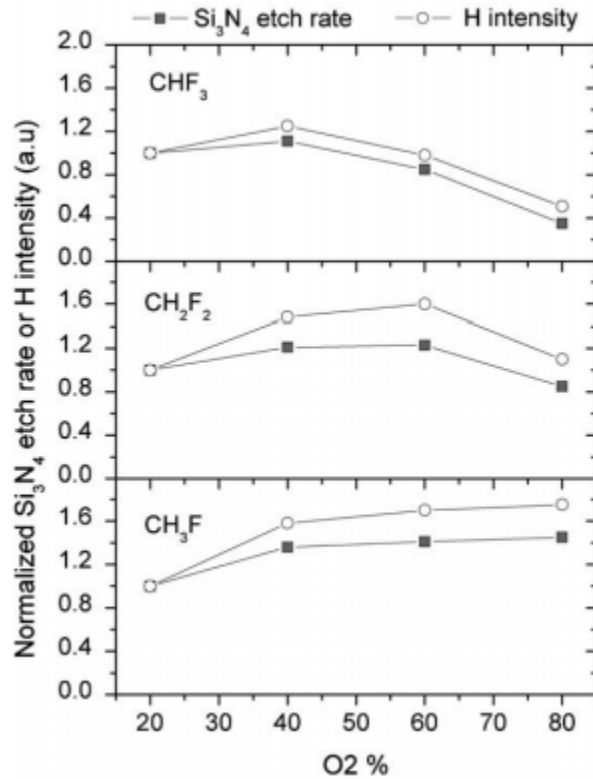
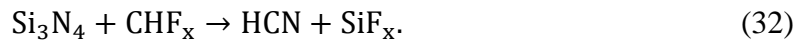


Fig. 9 Normalized H emission intensity and Si<sub>3</sub>N<sub>4</sub> etch rate versus O<sub>2</sub> % increase in fluorocarbon gases<sup>32</sup>.



Since the Si<sub>3</sub>N<sub>4</sub> etch rates were measured to be faster than SiO<sub>2</sub> etch rates, the thickness of the polymer layer on Si<sub>3</sub>N<sub>4</sub> in these experiments should be less than the thickness of the etch inhibiting layer on SiO<sub>2</sub>. Excluding CHF<sub>3</sub> – possible role of ion-induced defluorination of fluorocarbon film<sup>35</sup> - this was indeed the case. Figure 10 has the polymer thickness (nm) versus hydro-fluorocarbon gas.

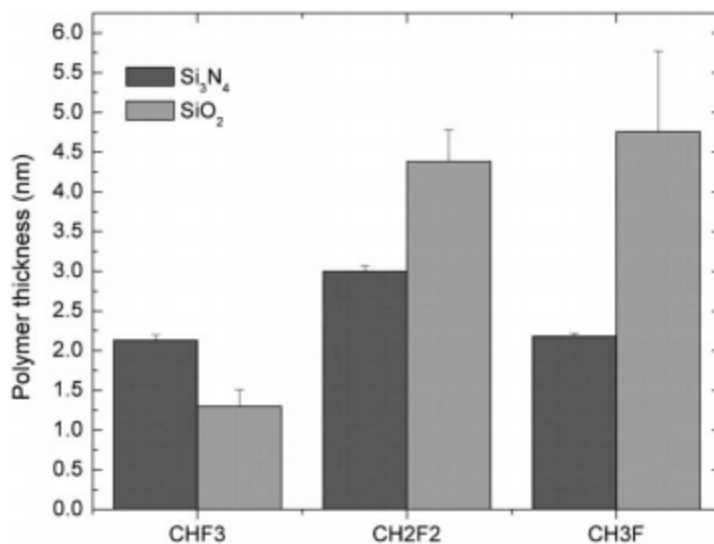


Fig. 10 Polymer thickness formed on etched surfaces in hydro-fluorocarbon Plasma<sup>32</sup>.

### 2.5 Polymer Films on SiN<sub>x</sub> after Etching with Hydro-Fluorocarbon Plasma.

Continuing with the experiments conducted by Chen et al., x-ray photoelectron spectroscopy spectra were obtained for partially etched Si<sub>3</sub>N<sub>4</sub> and SiO<sub>2</sub> substrates using CH<sub>3</sub>F/O<sub>2</sub> plasma<sup>32</sup>. The Si 2p, C 1s, F 1s, N 1s, and O 1s peaks were of primary focus shown in figure 11.

The polymer film on Si<sub>3</sub>N<sub>4</sub> contains C-C, C-H, and a very small amount of C-CF<sub>x</sub>. In contrast, the polymer film on SiO<sub>2</sub> includes C-C, C-H, and a much larger amount of C-CF<sub>x</sub> bonds. The integrated area of C 1s was larger on the SiO<sub>2</sub> substrate, indicating a thicker polymer film<sup>32</sup>. Chen et al. also noticed the difference in Si/N ratio, before and after etching. The Si/N ratio was .75, originally. This value decreased after exposing the Si<sub>3</sub>N<sub>4</sub> substrate to various hydro-fluorocarbon plasmas, suggesting SiF<sub>x</sub> products are removed at a faster rate than N atoms<sup>32</sup>. Park et al. gave evidence that the N atom removal from a Si<sub>3</sub>N<sub>4</sub> wafer is one of the major rate limiting step<sup>33</sup>.

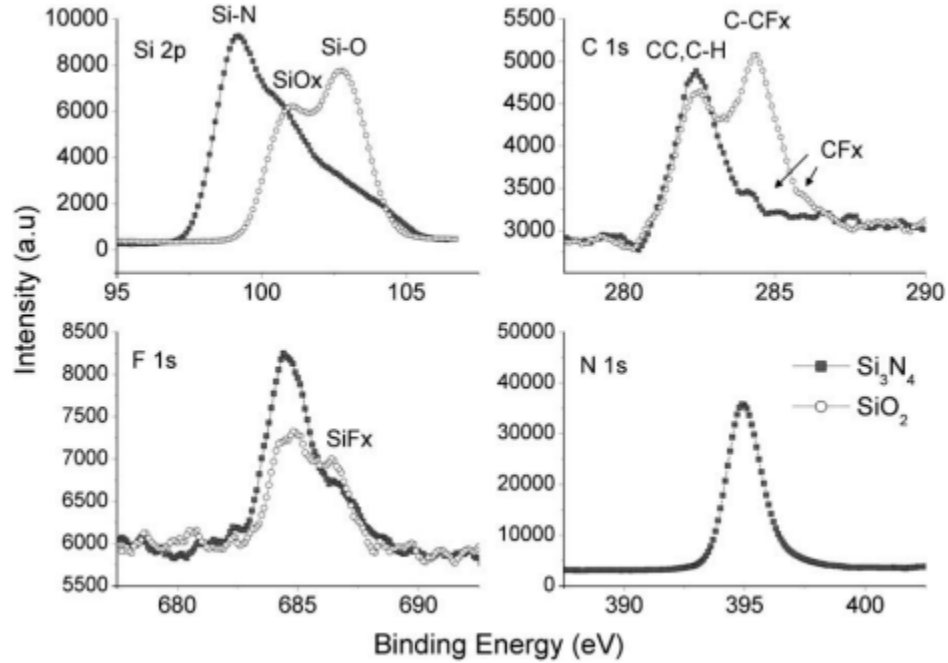


Fig. 11 XPS spectra after etching  $\text{Si}_3\text{N}_4$  and  $\text{SiO}_2$  with  $\text{CH}_3\text{F}/\text{O}_2$  plasma<sup>32</sup>.

Figure 12 has the  $\text{Si}_3\text{N}_4$  etch rate and  $\text{CH}_x\text{F}_y$  polymer thickness as a function of  $\text{H}_2$  flow rate addition to feed  $\text{CH}_2\text{F}_2 + \text{Ar}$  - examined by Park et al.<sup>33</sup>. The reduction of steady state  $\text{CH}_x\text{F}_y$  film thickness was attributed to the removal of hydro-fluorocarbon layer by the formation of  $\text{HCN}$  and  $\text{SiF}_x$  molecules with increasing  $\text{H}_2$ <sup>33-36</sup>. Ultimately,  $\text{Si}_3\text{N}_4$  etch rates were enhanced. Though the selective etching of  $\text{Si}_3\text{N}_4$  was heavily dependent on the hydro-fluorocarbon film thickness, Standaert et al. studied the significance of ion-induced defluorination of the polymer film, resulting in a difference of F/C ratio – which may affect  $\text{Si}_3\text{N}_4$  etch rates<sup>35</sup>.

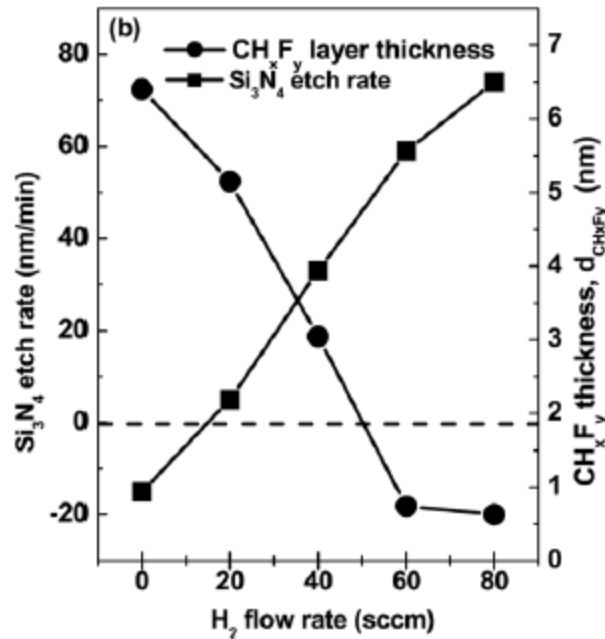


Fig. 12  $\text{Si}_3\text{N}_4$  etch rate and hydro-fluorocarbon film thickness versus  $\text{H}_2$  flow rate addition to  $\text{CH}_2\text{F}_2 + \text{Ar}^{33}$ .

Standaert et al.<sup>35</sup> investigated the role of fluorocarbon and hydro-fluorocarbon film formation in the etching of Si,  $\text{SiO}_2$ , SiCH, and  $\text{SiN}_x$  while varying substrate self-biased voltage (-V). Their plot relating etch rate with polymer film thickness is referenced in figure 13.

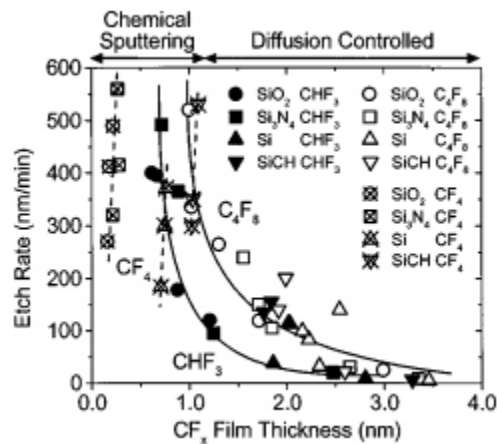


Fig. 13 Etch rates of  $\text{SiO}_2$ ,  $\text{Si}_3\text{N}_4$ , SiCH, and Si in multiple fluorocarbon plasmas as a function of self-biased voltage.  $\text{CF}_x$  film thicknesses were measured<sup>35</sup>.

The gases in the plot above were  $\text{CF}_4$ ,  $\text{CHF}_3$ , and  $\text{C}_4\text{F}_8$ , where each deposited 5, 250, and 330 nm/min of fluorocarbon (FC) film on Si, respectively<sup>35</sup>. The difference in deposition rates are strongly dependent on polymerization, therefore, the discharges with a lower F/C ratio would deposit at a much higher rate – creating larger FC films<sup>35</sup>. For  $\text{CF}_4$ , as self-biased voltage on the substrate holder increased, the  $\text{Si}_3\text{N}_4$  etch rate increased, but the polymer film thickness did not increase. In contrast, when self-bias increased from -45 to -200 V for  $\text{CHF}_3$  and  $\text{C}_4\text{F}_8$  plasma, the FC film thickness increased and etch rates decreased.

The etching rates are vertical in the chemical-sputtering region - where the film thickness was less than 1.2 nm. Here, etch rates are independent of film thickness and dependent on self-bias<sup>35</sup>. The ‘chemical sputtering’ region is, thus, less dependent on film thickness and more dependent on the ion energy<sup>35</sup>. They consider this the region where most ions penetrate the FC film possibly causing defluorination of the FC film, resulting in higher etch rates (higher probability of forming more  $\text{SiF}_x$  products desorbing from Si substrates)<sup>35</sup>. The ‘Diffusion controlled’ region has a different effect. Once FC thickness had increased 1.2 nm, the etch rates sharply decreased. Etch rate values are much smaller at larger FC thicknesses due to less ion induced penetration/fragmentation/defluorination and less diffusion of H or F for the formation of HCN and/or FCN.

## Chapter 3 Experimental

### 3.1 Apparatus

An inductively coupled plasma was ignited in a 1.4" inner diameter alumina tube, surrounded by a 3 turn, 1/4" outer diameter copper tubing, and housed in a 4" outer diameter co – axial stainless steel cylindrical enclosure (figure 14). Deionized (DI) water flowed through Teflon tubing around the exterior wall of the alumina tube providing cooling. A chiller maintained the DI water temperature of 20° C.

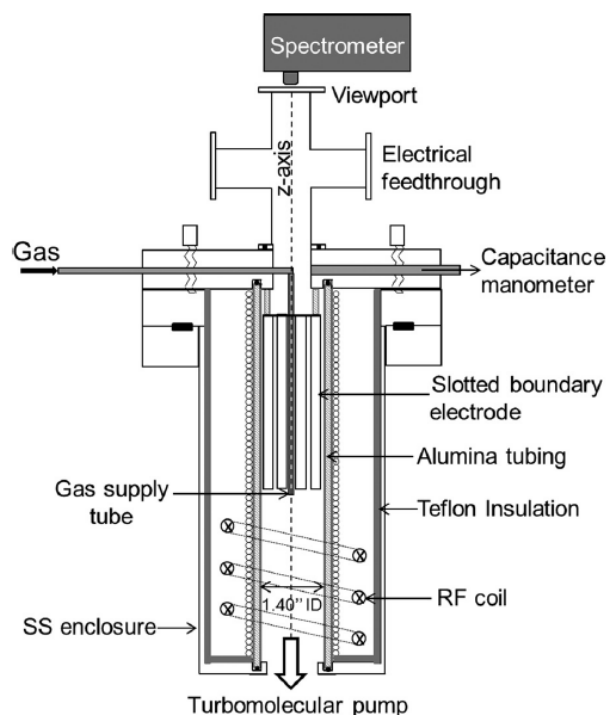


Fig. 14 Schematic of compact, inductively coupled plasma source.

Gas was fed into a reactor through a 1/4" stainless steel tube which was connected to a gas manifold. Flows of CH<sub>3</sub>F, CO<sub>2</sub>, O<sub>2</sub> and a trace rare gas (TRG) mixture (40% Ne, 20% Ar, 20% Kr, and 20% Xe) were controlled by MKS model 1179A mass flow controllers. The reactor was pumped by a 300 l/s turbomolecular pump – (Ebara

Corporation) backed by a dry pump. A base pressure of  $3.0 \times 10^{-8}$  Torr was measured using a Varian (model XGS-600) controller and Ion Gauge. The operating pressure, measured with a capacitance manometer at the top of the reactor, was maintained constant at 10 mTorr via a throttle valve.

Power was supplied to the ICP coil using a Hewlett-Packard (model 3325A) frequency synthesizer set at 13.56 MHz and ENI (model A-300) radio frequency (rf) power amplifier. With a  $\pi$ -impedance-matching network, a forward power of 300 W could be maintained with zero reflected power. Power was measured with in-line Bird-meters. A programmable DC power supply (Kepco model KLP 150-16- 1200 Watt) was connected onto the substrate holder, allowing ion energy control by applying either a positive (to slow or stop positive ions) or negative (to promote energetic ion bombardment) bias.

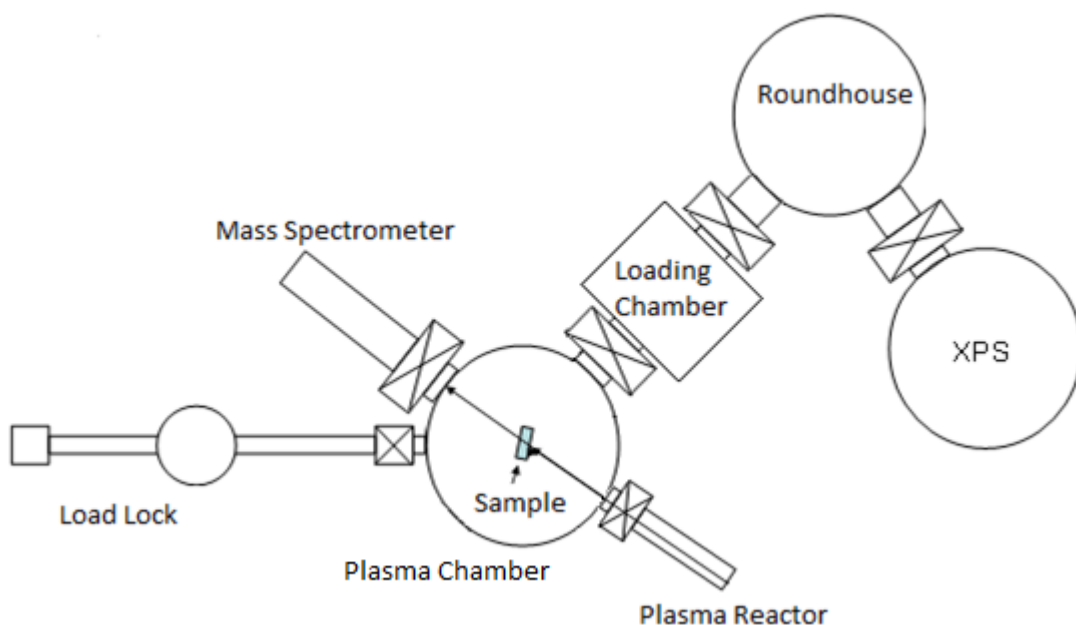


Fig. 15 Top view schematic of the overall system consisting of a plasma chamber, load lock chamber, ICP plasma reactor, mass spectrometer, and XPS.

The processing chamber was connected to a Physical Electronics' Model 10-420 X-ray photoelectron spectrometer (XPS) and Hiden Analytics EQP model 7036 mass spectrometer (MS). Samples were introduced into a loading chamber between the roundhouse and plasma chamber. The XPS and Roundhouse chambers were each pumped by a separate ion pump (Gamma Vacuum model Titan<sup>TM</sup> 300TV) achieving base pressures of  $3.0 \times 10^{-9}$  Torr.

The loading chamber was purged with dry nitrogen when inserting or removing a sample. The substrate sample holder was moved between chambers with transfer arms, where each chamber could be isolated by gate valves. The samples used in this study were 300 nm SiN<sub>x</sub> on Si, 10 nm Si on a 1000 nm Ge on a Si substrate, or a p-type Si wafer. Samples were cleaved into 3 cm pieces and held on the sample holder with conductive carbon tape. The Si/Ge and Si substrate samples were dipped into 50% dilute HF solution before mounting for the removal of the native oxide layer (SiO<sub>2</sub>).

### **3.2 X-Ray Photoelectron Spectroscopy**

Quantitative chemical analysis of plasma-exposed wafers was carried out with XPS. XPS spectra were collected for 70 cycles, with a 0.05 eV/step for high resolution scans. The Ge 3d (29.4 eV), Si 2p (99.3 eV), C 1s (284.5 eV), N 1s (398.1 eV), O 1s (531 eV), and F 1s (684.9 eV) regions were of primary focus.

XPS was also used to determine the thickness of films that were etched or deposited. Etching and deposition rates were then determined from thickness changes. The method was based on measuring the relative intensity of peaks from the film, which increased as the film thickened and those from the underlying substrate, which decreased as the polymer film thickened.<sup>37, 38</sup> For Si on Ge, the Si thickness is given by

$$t_{\text{Si}} = \lambda_{\text{Si}} \sin \theta \cdot \ln \left[ 1 + \frac{I_{\text{Si}}}{I_{\text{Ge}}} \cdot \frac{\lambda_{\text{Ge}}}{\lambda_{\text{Si}}} \cdot \frac{n_{\text{Ge}}}{n_{\text{Si}}} \cdot \frac{S_{\text{Ge}}}{S_{\text{Si}}} \right]. \quad (33)$$

$\lambda_{\text{Ge}}$  and  $\lambda_{\text{Si}}$  are electron inelastic mean free path of 2.35 nm<sup>43</sup> and 2.2 nm<sup>37,38</sup>.  $\theta$  is the angle between the sample surface plane and the axis of the photoelectron collection lens, 90°.  $n_{\text{Ge}}$  and  $n_{\text{Si}}$  are the atom densities for Ge (4.44 x 10<sup>22</sup> cm<sup>-3</sup>) and Si (5.0 x 10<sup>22</sup> cm<sup>-3</sup>), respectively<sup>37,38</sup>.  $I_{\text{Ge}}$  and  $I_{\text{Si}}$  are the integrated intensities of Ge(3d) and Si(2p), respectively, and  $S_{\text{Ge}}$  and  $S_{\text{Si}}$  are the sensitivity factors for Ge and Si<sup>37,38</sup>. Note that the underlying Ge film is too thick for photoelectrons from the Si substrate underneath the Ge film to contribute to the Si signal. For the thickness of the polymer deposited on Si

$$t_{\text{c}} = \lambda_{\text{c}} \sin \theta \cdot \ln \left[ 1 + \frac{3 \cdot I_{\text{c}}}{I_{\text{Si}}} \cdot \frac{\lambda_{\text{Si}}}{\lambda_{\text{c}}} \cdot \frac{n_{\text{Si}}}{n_{\text{c}}} \cdot \frac{S_{\text{Si}}}{S_{\text{c}}} \right]. \quad (34)$$

Here the stoichiometry of the polymer film was assumed to be C:(H+O+F) = 1:2 and the carbon atom density was assumed to be that of polyethylene.  $\lambda_{\text{c}}$  is the electron inelastic mean free path of 4.1 nm<sup>43</sup>.  $n_{\text{c}}$  is the atom densities for polymer thickness deposited on Si assumed to be 3.9 x 10<sup>22</sup> cm<sup>-3</sup>.  $S_{\text{c}}$  and  $I_{\text{c}}$  are the sensitivity factor and integrated intensity of C(1s). Since H was not measured, there is considerable uncertainty in the absolute thickness of the polymer films, but comparisons of relative deposition rates under different conditions are valid. Polymer film thickness deposited on SiN<sub>x</sub> is given by<sup>37,38</sup>

$$t_{\text{c}} = \lambda_{\text{c}} \sin \theta \cdot \ln \left[ 1 + \frac{3 \cdot I_{\text{c}}}{\frac{7}{3} I_{\text{Si}}} \cdot \frac{\lambda_{\text{Si}_3\text{N}_4}}{\lambda_{\text{c}}} \cdot \frac{n_{\text{Si}_3\text{N}_4}}{n_{\text{c}}} \cdot \frac{S_{\text{Si}}}{S_{\text{c}}} \right]. \quad (35)$$

Where SiN<sub>x</sub> was assumed to have a stoichiometry of Si<sub>3</sub>N<sub>4</sub>.  $\lambda_{\text{Si}_3\text{N}_4}$  is the electron inelastic mean free path of for Si<sub>3</sub>N<sub>4</sub> of 2.7 nm<sup>43</sup>.  $n_{\text{Si}_3\text{N}_4}$  is the atom densities for Si<sub>3</sub>N<sub>4</sub> 1.48 x 10<sup>22</sup> cm<sup>-3</sup>.  $S_{\text{Si}_3\text{N}_4}$  and  $I_{\text{Si}_3\text{N}_4}$  are the sensitivity factor and integrated intensity of Si(2p).

### **3.3 Optical Emission Spectroscopy**

One of three Ocean Optics model HR4000 high resolution spectrometers was positioned at the top of the plasma source, with the entrance slit on the z-axis of the discharge tube and no intervening optical lenses (see figure 14). The three spectrometers covered wavelength ranges of 200-427, 578 – 775, and 734-916 nm, respectively. Sharp cut filters were used to block second order dispersion for the latter two spectrometers. Second order dispersion of the 734-916 nm region was used to obtain spectra between 367 – 458 nm. A colored glass filter, Kopp4305, was used to block first order dispersion in this case. The spectral resolution was 0.14 to 0.17 nm in first order and .07 nm in second order.

### **3.4 Mass Spectrometer**

The processing was connected to the mass spectrometer (MS) by two 4” nipples separated by an aperture and gate valve. The MS chamber contained an ionizer, chopper, and a Hiden Analytics MS EQP (model 7036) probe. Two stages of differential pumping were created with a turbo molecular pump ( $\sim 1 \times 10^{-7}$  Torr) in the chamber closest to the processing chamber and a Cryogenics Helix Technology corporation (model 100CryoTorr) cryopump ( $\sim 1 \times 10^{-9}$  Torr) in the second chamber.

### **3.5 Spectroscopic Ellipsometry**

Silicon nitride film thickness was measured before and after etching using a spectroscopic ellipsometry. The ellipsometer (J.A. Woollam Co. model M-2000S) was operated at a fixed angle of incidence  $55^{\circ}$  (micrometer angle 15 mm) over a wavelength range of 200-90 nm. A theoretical model of the sample was created within the ‘WVASE32’ or VASE-equipped software.

## Chapter 4 Results and Discussions

### 4.1 Selected Optical Emission Measurements

In a previous study from this laboratory, abrupt transitions in optical emission intensities were noted when oxygen addition to methyl fluoride reached 48% in a 300 W ICP at a pressure of 10 mTorr, and constant flow rate of 10 sccm.<sup>40,41</sup> These measurements were repeated in CH<sub>3</sub>F/O<sub>2</sub> plasmas and extended to CH<sub>3</sub>F/CO<sub>2</sub> plasmas.<sup>42</sup> Emission intensity and number density ratios to either Ar or Xe, normalized to unity at a particular dilution (usually for pure CH<sub>3</sub>F), are plotted as a function of CO<sub>2</sub> or O<sub>2</sub> addition with a constant total flow rate of 10.3 sccm, including 0.3 sccm TRG, at a pressure of 10mTorr and a power of 300W in figures 16-18.

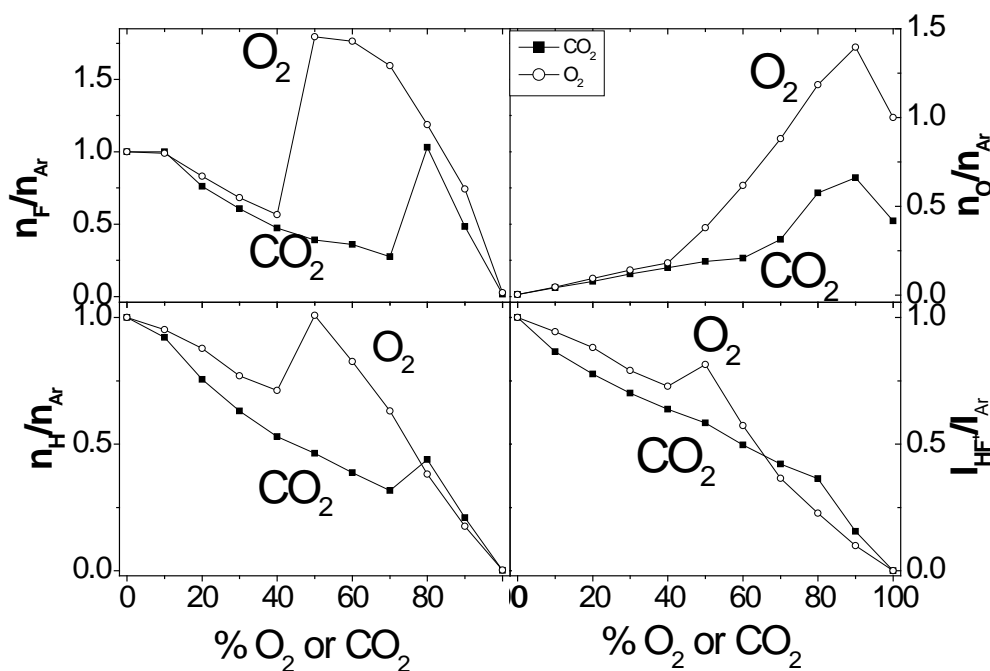


Fig. 16 Normalized number densities for  $(n_H/n_{Ar})/80.36$ ,  $(n_F/n_{Ar})/2.89$  and  $(n_O/n_{Ar})/24.58$ , and normalized intensity ratios for HF<sup>+</sup>/Ar, as a function of CO<sub>2</sub> or O<sub>2</sub> addition<sup>42</sup>.

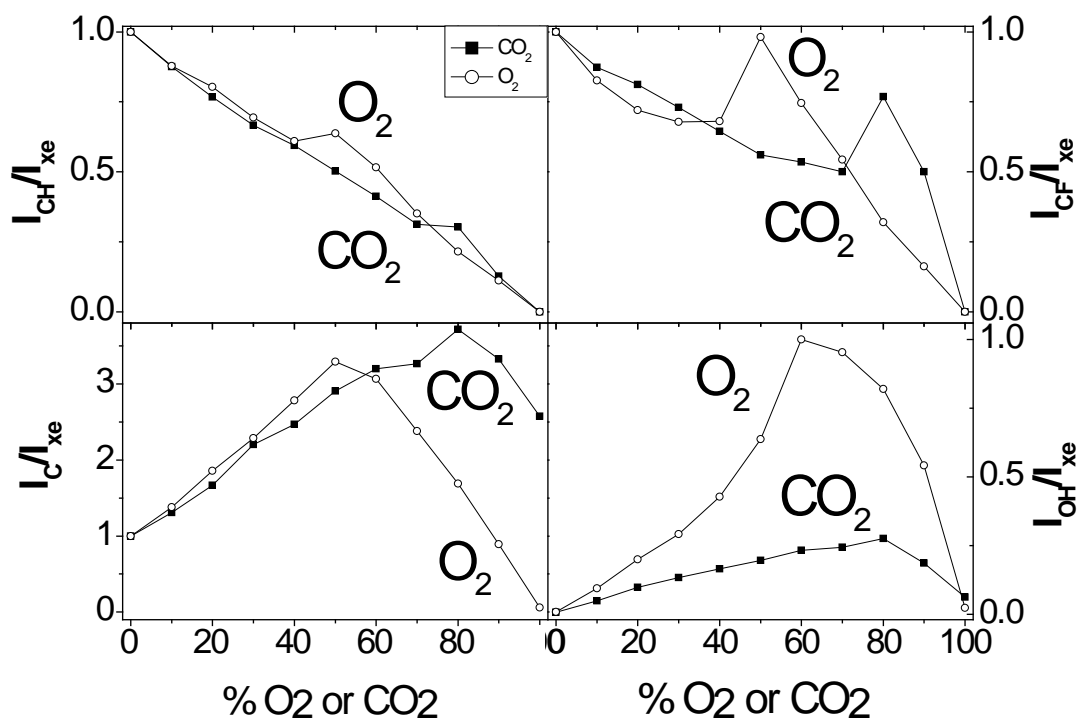


Fig. 17 Normalized intensity ratios of CH/Xe, CF/Xe, C/Xe, and OH/Xe emission as function of CO<sub>2</sub> or O<sub>2</sub> addition<sup>42</sup>.

In figure 16, normalized number densities for  $n_{\text{H}}/n_{\text{Ar}}$ ,  $n_{\text{O}}/n_{\text{Ar}}$ , and  $n_{\text{F}}/n_{\text{Ar}}$  are plotted for both O<sub>2</sub> and CO<sub>2</sub>. Expected dilution trends are observed independent of added gas, until sharp increases in number densities are noticed at 48% O<sub>2</sub> and 73% CO<sub>2</sub> addition. Both phenomena were attributed to the transition from a polymer-covered to polymer-free reactor wall conditions when exceeding the transition gas composition<sup>40-42</sup>. Figures 16-17 contain species F/Ar, H/Ar, C/Xe, CH/Xe, CF/Xe, HF+/Ar and CO/Ar number densities or emission ratios which were similar in trend at less than 40% O<sub>2</sub> or CO<sub>2</sub><sup>42</sup>. One clear difference between the two plasmas was observed in OH/Xe emission intensity (figure 17).

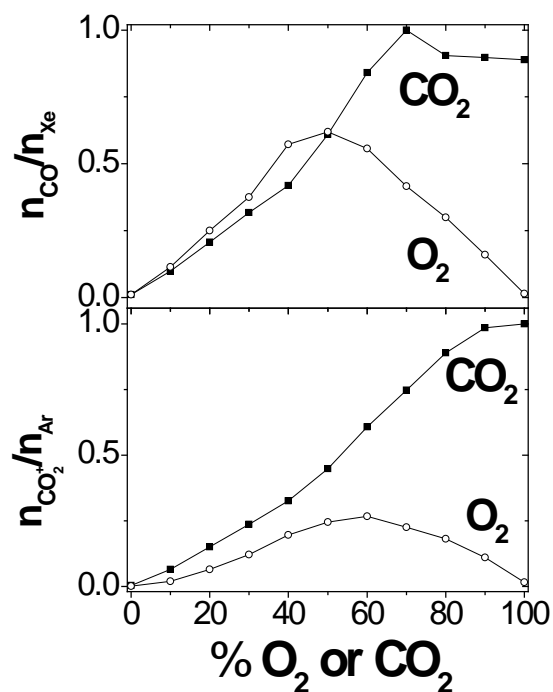


Fig 18. Normalized number densities for  $(n_{\text{CO}}/n_{\text{Xe}})/84.35$  and  $(n_{\text{CO}_2^+}/n_{\text{Ar}})/27.59$  as a function of  $\text{CO}_2$  or  $\text{O}_2$  addition<sup>42</sup>.

$\text{OH}/\text{Xe}$  emission was lower in  $\text{CH}_3\text{F}/\text{CO}_2$  than in  $\text{CH}_3\text{F}/\text{O}_2$  plasmas as a function of  $\text{O}_2$  and  $\text{CO}_2$  addition<sup>42</sup>. In the region greater than 80%  $\text{O}_2$  or  $\text{CO}_2$ ,  $\text{O}$  number density was about twice in  $\text{CH}_3\text{F}/\text{O}_2$  plasmas than in  $\text{CH}_3\text{F}/\text{CO}_2$  plasmas<sup>42</sup>. Another key difference, in figure 18, was the larger  $\text{CO}_2^+$  number density in  $\text{CH}_3\text{F}/\text{CO}_2$  plasmas<sup>42</sup>.

$\text{C}/\text{Xe}$  emission ratios are identical in both plasmas up until 60% addition of  $\text{O}_2$  and  $\text{CO}_2$ <sup>42</sup>. After exceeding 60%  $\text{O}_2$  addition,  $\text{C}/\text{Xe}$  emission dropped linearly until the feed was of pure  $\text{O}_2$ . This was identical to the behavior of  $\text{CO}$  and  $\text{CO}_2^+$  number density as a function of  $\text{O}_2$  addition. With  $\text{CO}_2$  addition, however,  $\text{C}/\text{Xe}$  emission was maintained about constant. Due to the similar trend in  $\text{CO}/\text{Xe}$  and  $\text{C}/\text{Xe}$  emission versus

CO<sub>2</sub> addition, C atoms may have been formed through dissociative excitation of CO, as well as electron impact on C produced from dissociation of CO<sup>42</sup>.

H atom number density appears to be the most abundant species measured using self-actinometrical calculations. This was further confirmed with mass spectrometry. The characterization of a CH<sub>3</sub>F/O<sub>2</sub> 1:1 ratio, 10 sccm gas and plasma (300W) were compared. Shown in figure 19, MS spectra were initially recorded of the feed mixture, and then again after supplying power to the 3 turn, ICP copper coil within the plasma reactor.

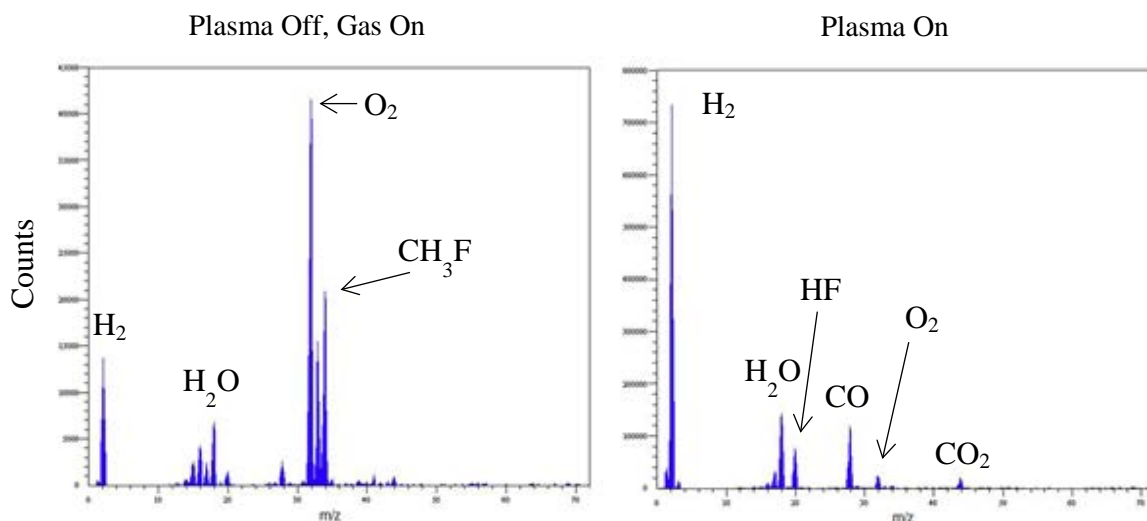


Fig. 19 Mass spectrometry suggests nearly complete dissociation of CH<sub>3</sub>F into smaller, stable products.

Gas mass-to-charge (m/z) peaks detected were of parent molecules CH<sub>3</sub>F, O<sub>2</sub>, and H<sub>2</sub>O. After the plasma was on, near complete dissociation of CH<sub>3</sub>F and its conversion to products H<sub>2</sub>, CO, HF, and CO<sub>2</sub> were found. A sharp increase in H<sub>2</sub> counts (52.8 fold) suggests large conversion to H<sub>2</sub>, maybe due to recombination third body reactions off of MS chamber walls. All MS data were obtained without the use of a chopper and proper line-of-sight.

## 4.2 Deposition of Polymer on Si with CH<sub>3</sub>F/O<sub>2</sub> and CH<sub>3</sub>F/CO<sub>2</sub> Plasma

Polymer films were deposited on Si using the polymer heavy side of the transition composition (<80% CO<sub>2</sub> and <50 % O<sub>2</sub>). Samples were turned away from the plasma source for 20s to reach steady-state plasma conditions (300 W and 10 mTorr with no boundary bias) and then exposed to the plasma source for an additional 20s, or in some cases, 40s. Polymer-film growth rates, using the time that the samples were directly exposed to the plasma beam, were measured with x-ray photoelectron spectroscopy and with use of equation (17).<sup>49</sup> The results are shown in figure 20.

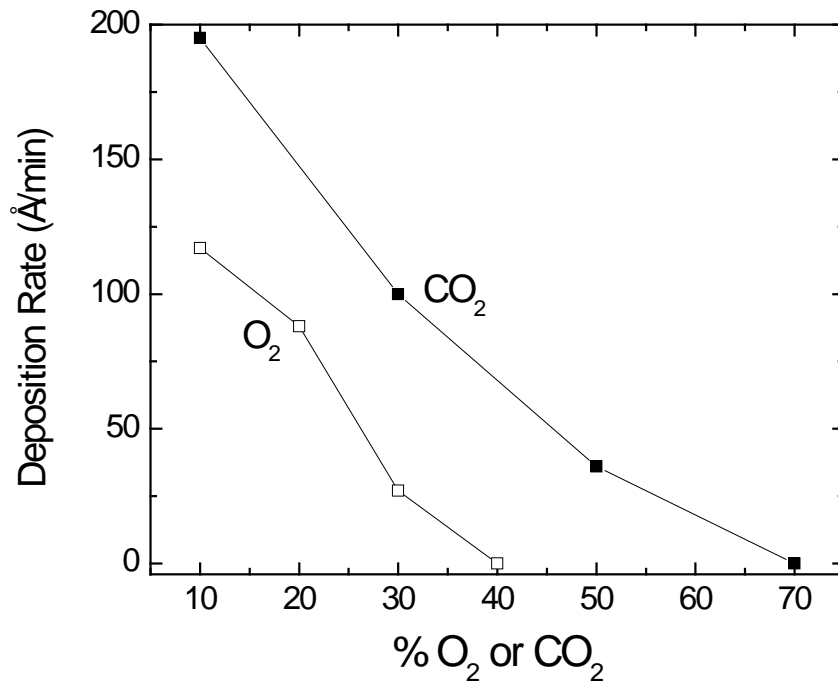
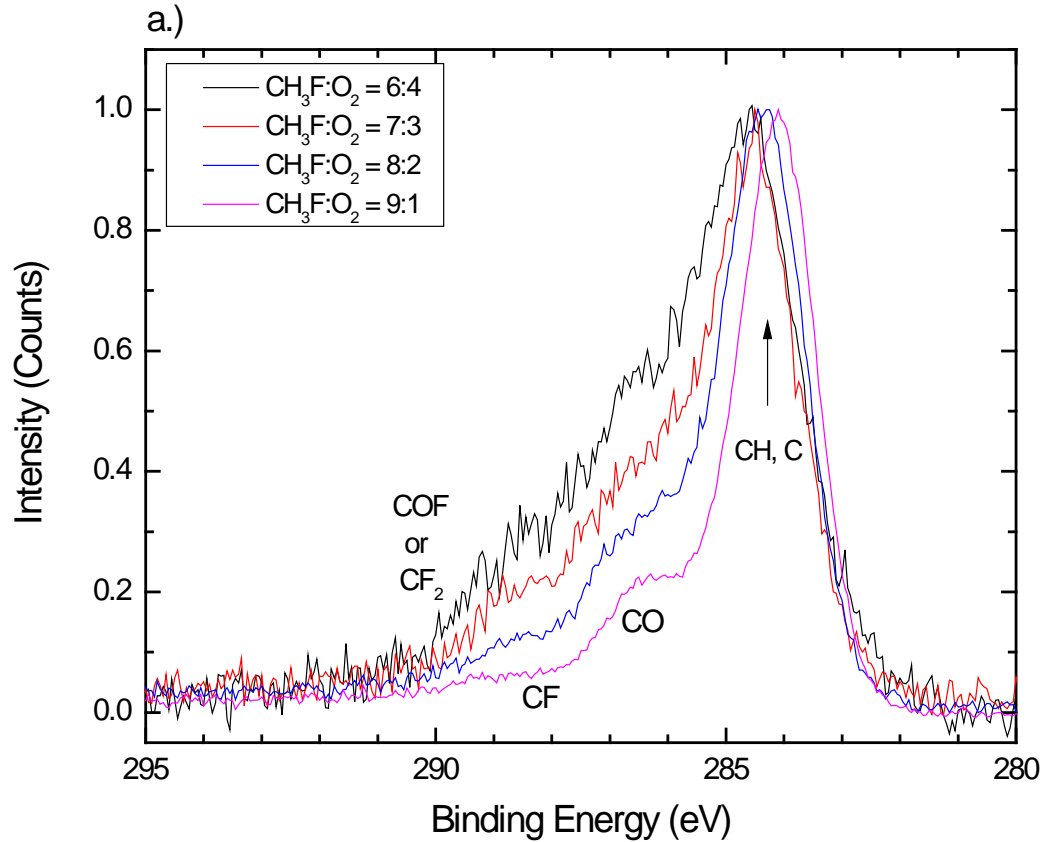


Fig. 20 Film deposition rates on p-Si for CH<sub>3</sub>F/O<sub>2</sub> and CH<sub>3</sub>F/CO<sub>2</sub> plasmas at 300 W, 10 mTorr, and no boundary bias<sup>42</sup>.

The film deposition rates decreased with increasing CO<sub>2</sub> and O<sub>2</sub> addition, approaching zero near 70% CO<sub>2</sub> and 40% O<sub>2</sub>. This supports the explanation for the abrupt increases in F and O number density observed in both plasmas at higher O<sub>2</sub> and

CO<sub>2</sub> additions - the polymer film is etched by O atoms at a rate higher than the deposition rate<sup>40-42</sup>. The C(1s) spectra, displayed in figures 21 a) and b), contained a sharp peak near 284.3 eV (CH, CH<sub>2</sub> and/or graphitic carbon) and weaker peaks at 286.4 eV (CO) and 289 eV (CF), with perhaps very weak CF<sub>2</sub> (or more likely CFO) feature near 290 eV.



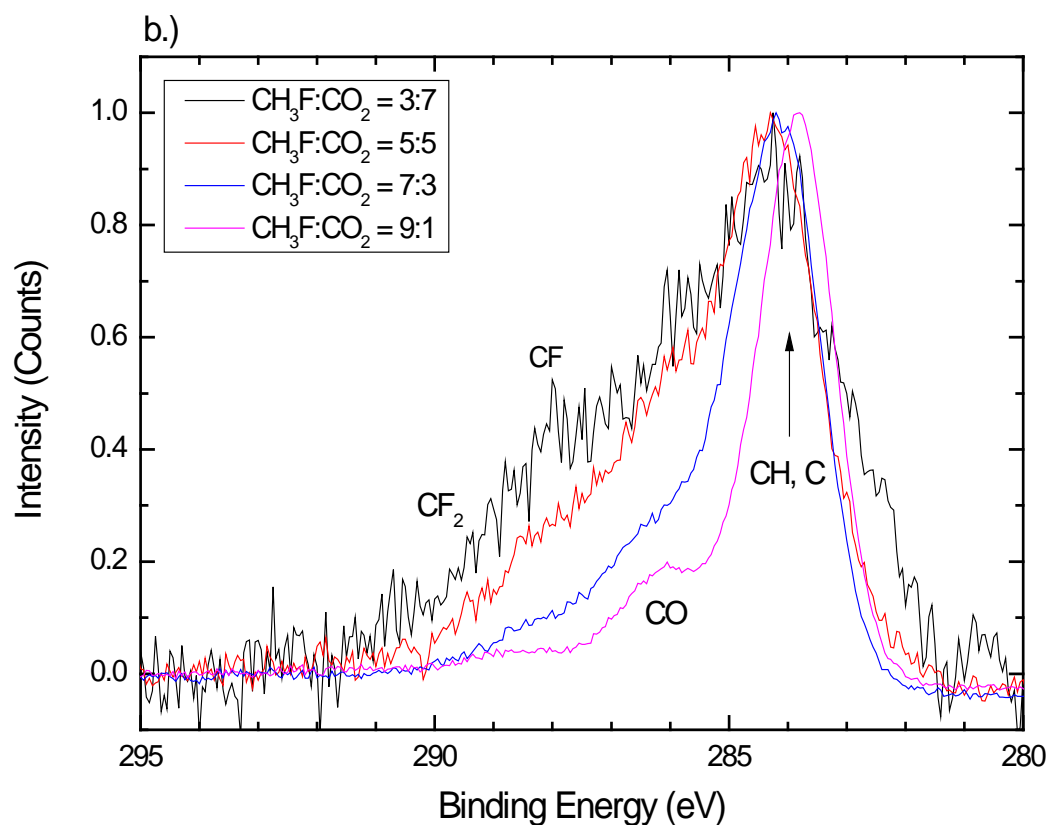


Fig. 21 The C (1s) spectra of deposited film on p-Si as a function of a.) CH<sub>3</sub>F/O<sub>2</sub> and b.) CH<sub>3</sub>F/CO<sub>2</sub> plasma<sup>42</sup>.

Figures 22 a) and b) shows the Si(2p) spectra with peaks at 99.5 eV (Si) and 103.7 eV (SiO<sub>2</sub>). The SiO<sub>2</sub> peak increases, relative to Si(2p), as a function of % O<sub>2</sub> and CO<sub>2</sub> addition as anticipated. Figures 23 a) and b) displays the O(1s) spectra. A shift towards higher binding energy of peak 532 eV was noticed as % O<sub>2</sub> and CO<sub>2</sub> increased, presumably due to the increased formation of CO and CF<sub>x</sub> or COF. The same effect was detected in the F(1s) XPS spectra for peak 686.2 eV, presented in figures 24 a) and b).

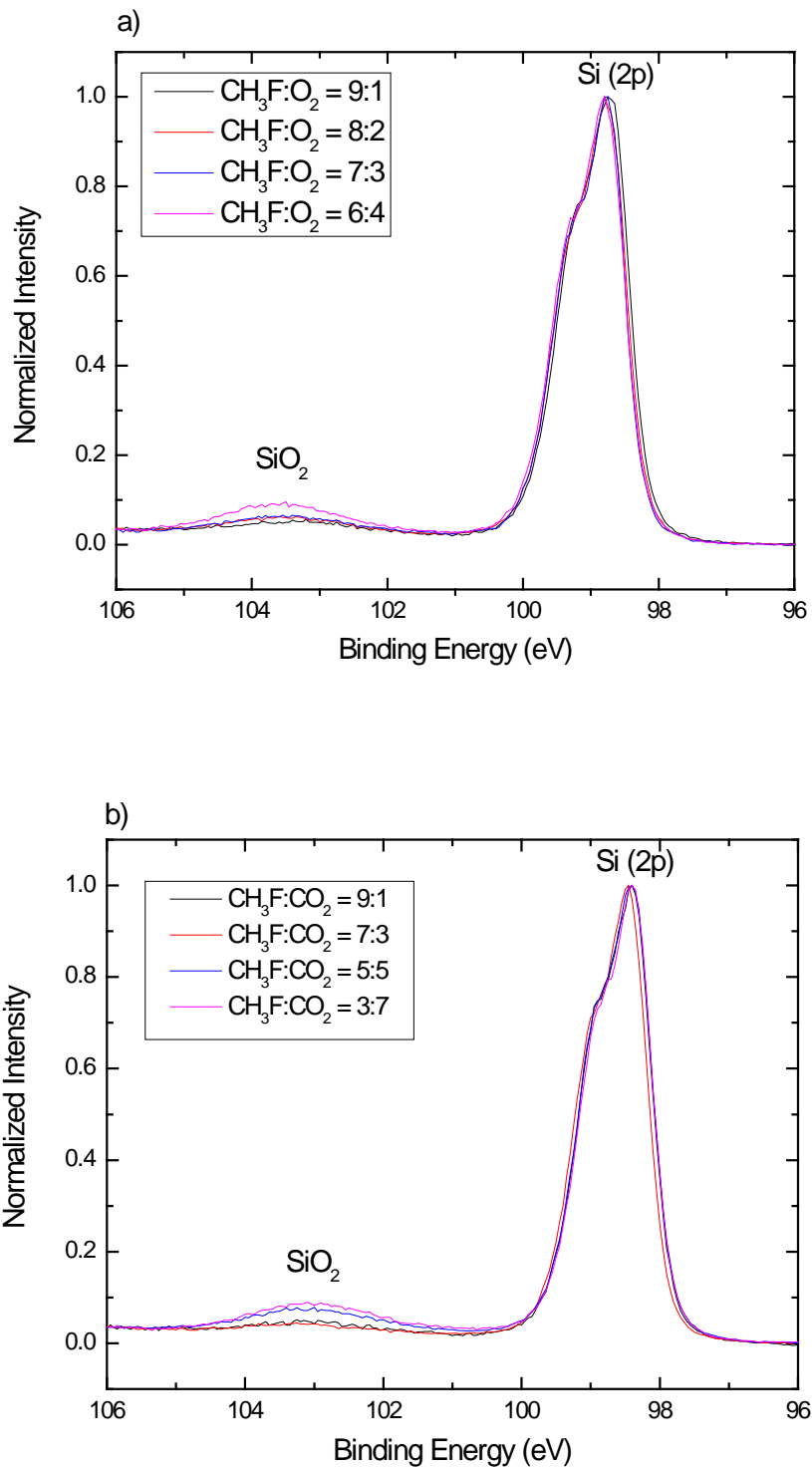


Fig. 22 The Si (2p) spectra of deposited film on p-Si as a function of a.) CH<sub>3</sub>F/O<sub>2</sub> and b.) CH<sub>3</sub>F/CO<sub>2</sub> plasma<sup>42</sup>.

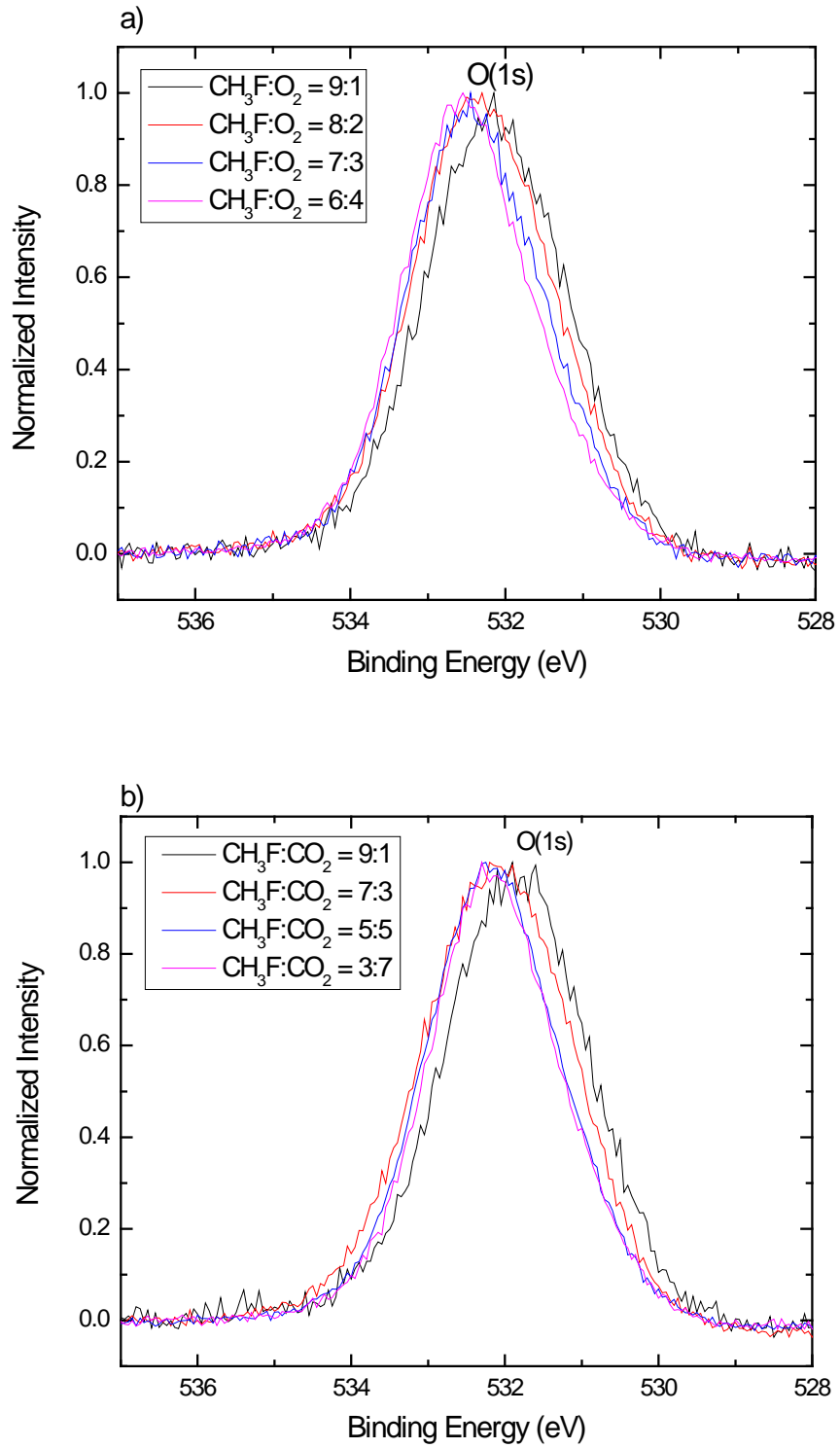


Fig. 23 The O (1s) spectra of deposited film on p-Si as a function of a.)  $\text{CH}_3\text{F}/\text{O}_2$  and b.)  $\text{CH}_3\text{F}/\text{CO}_2$  plasma<sup>42</sup>.

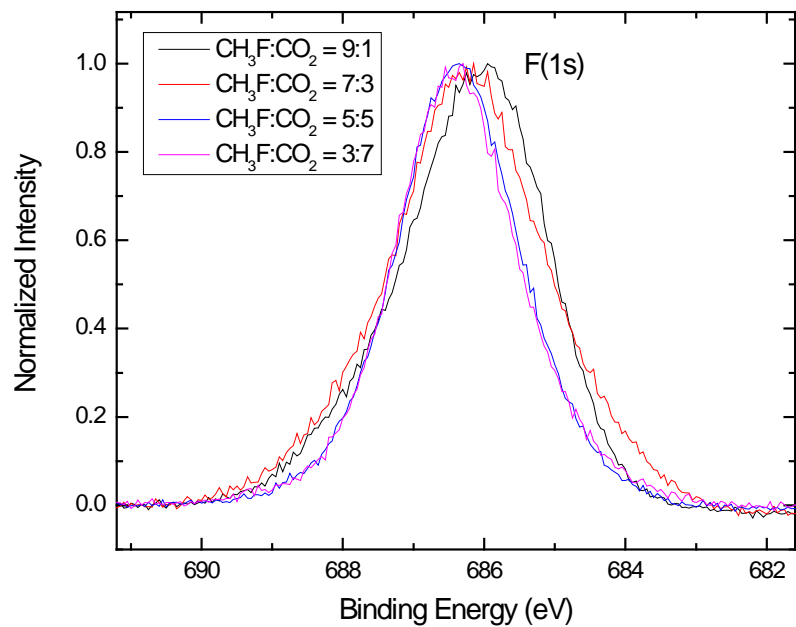
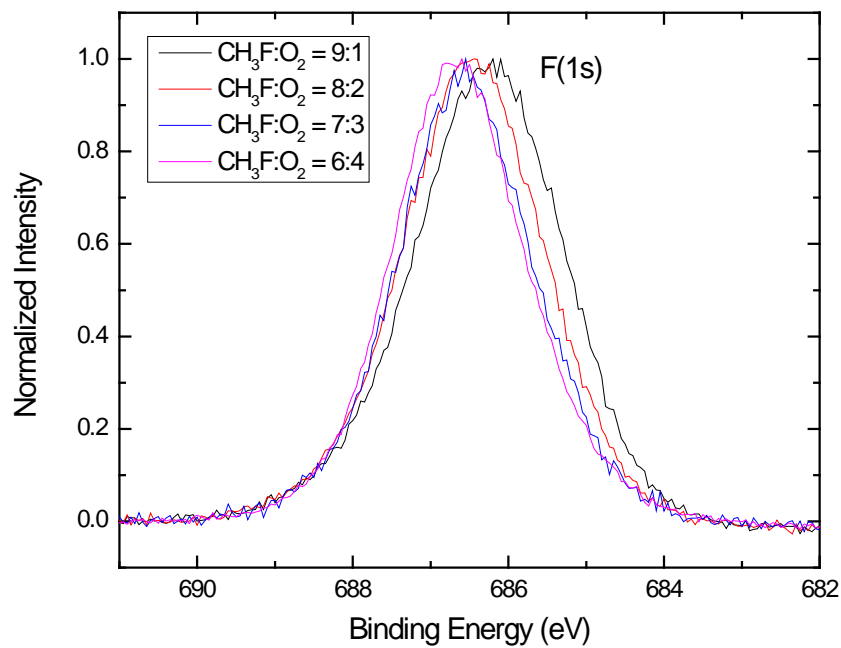


Fig. 24 The F (1s) spectra of deposited film on p-Si as a function of a.) CH<sub>3</sub>F/O<sub>2</sub> and b.) CH<sub>3</sub>F/CO<sub>2</sub> plasma<sup>42</sup>.

As O<sub>2</sub> and CO<sub>2</sub> addition increased in plasma, XPS peaks relative ratios CO<sub>286.4</sub> eV/C<sub>1s</sub> and CF<sub>288.8</sub> eV/C<sub>1s</sub> increased as expected<sup>42</sup>. Though CH<sub>3</sub>F/CO<sub>2</sub> produced higher film deposition rates, it can be concluded that there were no significant differences between the polymer-films deposited in CH<sub>3</sub>F/O<sub>2</sub> versus CH<sub>3</sub>F/O<sub>2</sub> plasmas (at similar deposition rates).<sup>42</sup> Perhaps the higher OH and or H<sub>2</sub>O levels in O<sub>2</sub>-containing plasmas suppresses deposition. Thermodynamic equilibrium also favors solid carbon formation in CH<sub>3</sub>F/CO<sub>2</sub> plasmas throughout all percentages of O<sub>2</sub> and CO<sub>2</sub> addition.<sup>42</sup>, as shown in figure 25<sup>42</sup> possibly explaining the higher film deposition rates.

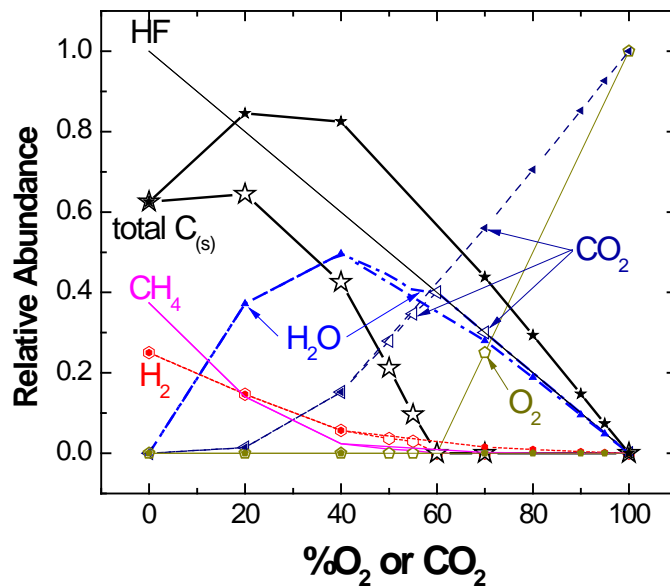


Fig. 25 Relative abundance of species at thermodynamic equilibrium in CH<sub>3</sub>F/O<sub>2</sub> (hole symbol) and CH<sub>3</sub>F/CO<sub>2</sub> (solid symbol) plasmas at 10 mTorr and a temperature of 373 K. Overlapping plots convey no difference in trends<sup>42</sup>.

#### 4.3 Etched Si on Ge with CH<sub>3</sub>F/O<sub>2</sub> and CH<sub>3</sub>F/CO<sub>2</sub> Plasmas

Si (10 nm) on Ge (1000 nm on Si substrates) samples were exposed to CH<sub>3</sub>F/CO<sub>2</sub> and CH<sub>3</sub>F/O<sub>2</sub> plasma beams at 300 W, 10 mTorr and a constant flow rate of 10 sccm.

Samples faced the plasma beam for 20s at 70%, 80%, and 85% CO<sub>2</sub>, 40s for 90% and 80s for 95% CO<sub>2</sub> - conditions for which the reactors walls were polymer free. For O<sub>2</sub>, wafers were exposed to the plasma beam for 20s versus O<sub>2</sub> % addition in the polymer-free wall condition (>50% O<sub>2</sub>). XPS analysis (equation (16)) revealed that the Si film was partially removed. It was noted (figure 26) that etching had stopped after the removal of ~ 30 Å of Si for both plasmas, independent of composition and time.

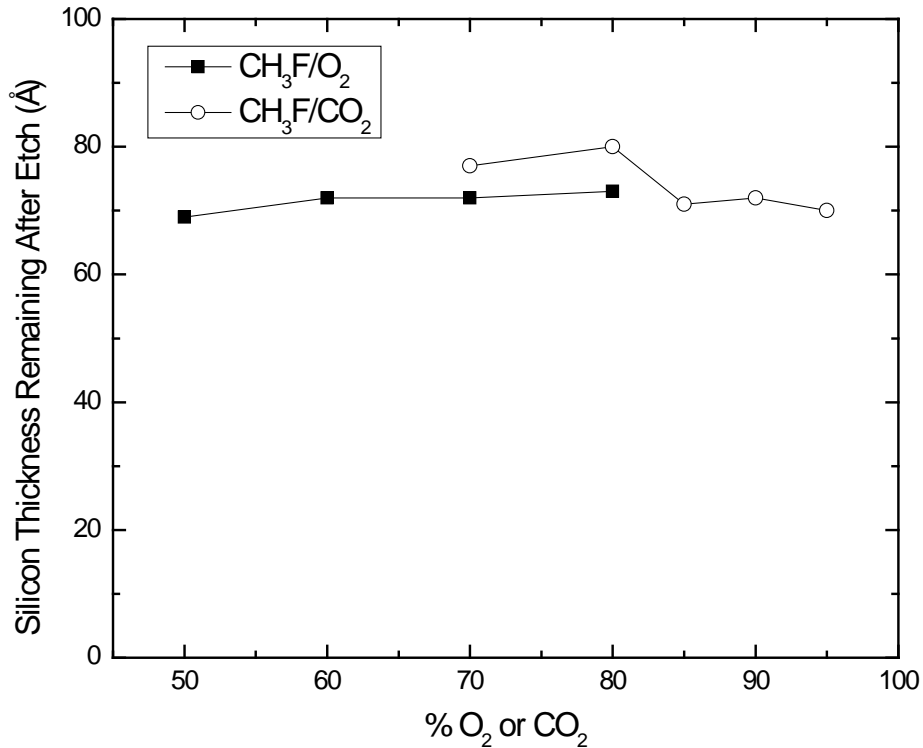


Fig. 26 Si thickness remaining on Ge after exposing to CH<sub>3</sub>F/O<sub>2</sub> (solid circles) and CH<sub>3</sub>F/CO<sub>2</sub> (open circles) plasmas at 300 W and 10 mTorr without boundary bias.

XPS spectra in the Si (2p) and Ge (3d) regions provide further insight. Initially, the spectra shown in figures 27 and 28 were recorded before the sample was dipped in HF solution. A native oxide layer was evident on top of the initial Si film. Ge (3d) can

easily be detected since the Si layer was very thin and the inelastic mean free path of Si at 1456.6 eV (the x-ray energy 1486 minus the Ge 3d binding energy) is 2.2 nm. Most significantly, there was no GeO<sub>2</sub> peak, indicating that the Si layer deposited on Ge was continuous and contained no open patches or pinholes. If any Ge were exposed, it would oxidize in the period of months that the Si/Ge wafer sat in open air.

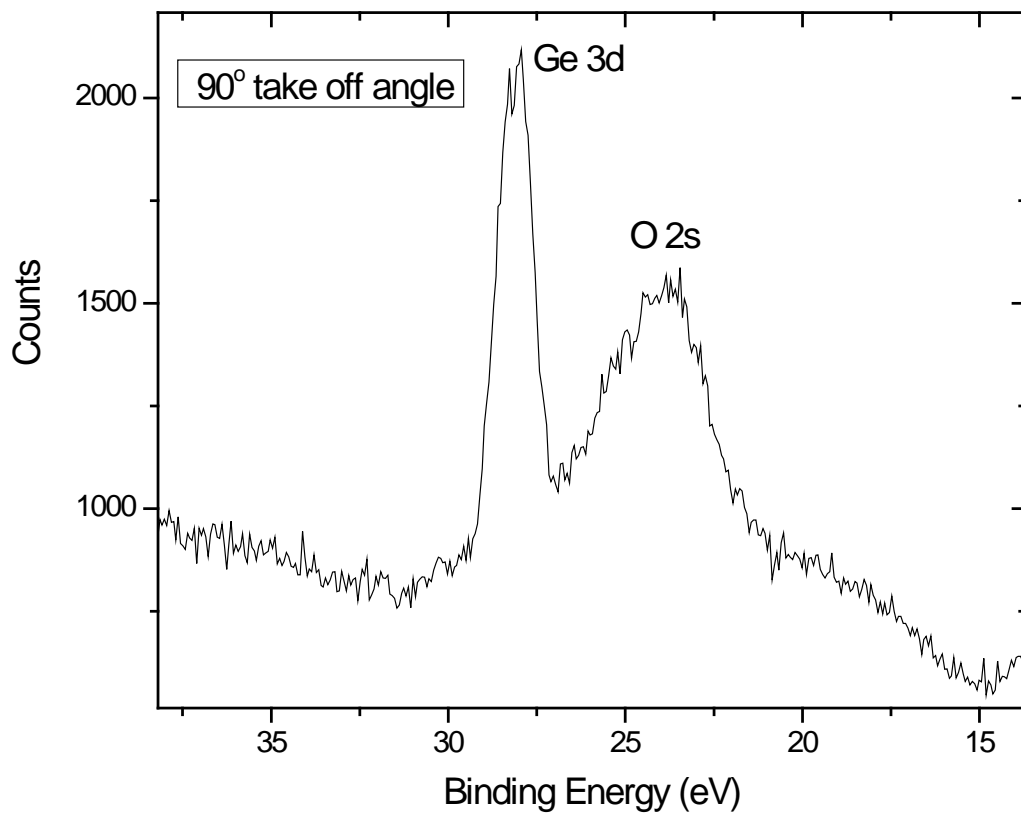


Fig. 27 Ge (3d) XPS spectrum of Si on Ge without HF dip.

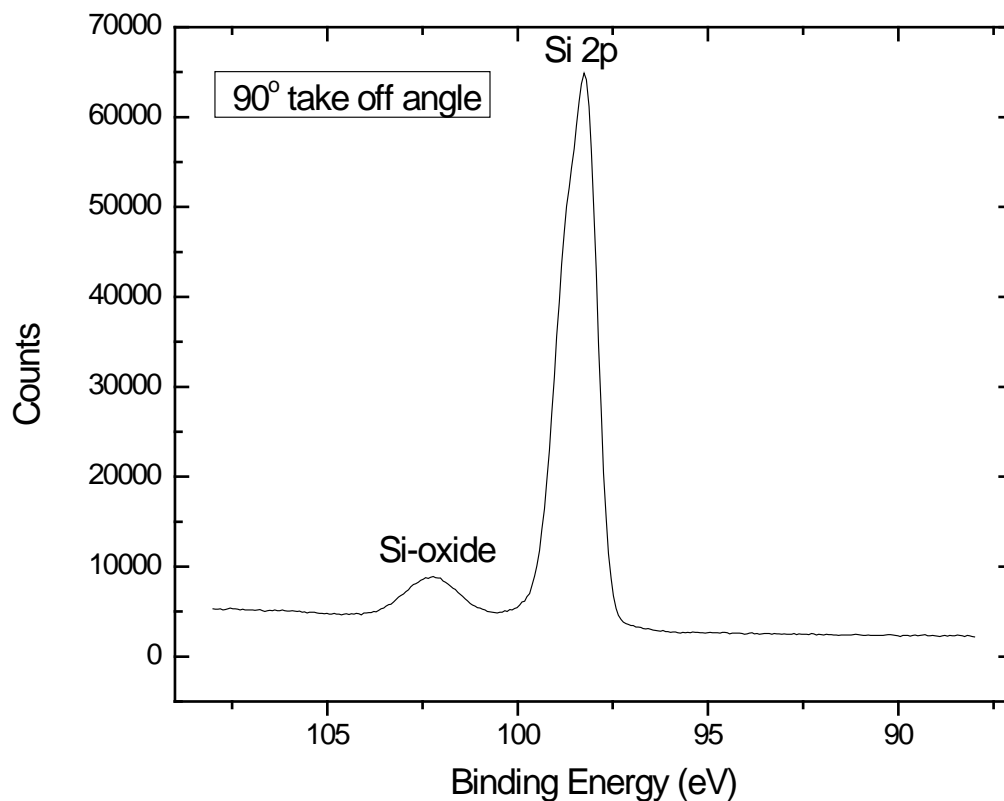


Fig. 28 Si (2p) XPS spectrum of Si on Ge without HF.

The substrate was then dipped in HF, removing the SiO<sub>2</sub> layer as was evident from the Si (2p) spectrum in figure 29 a.) and b.) - labelled as original. Separate HF-dipped samples were then exposed to plasma beams formed from plasmas with different O<sub>2</sub> and CO<sub>2</sub> addition. With Si (2p) normalized to unity, the relative oxide peak increased as the O<sub>2</sub> % or CO<sub>2</sub> % increased, as anticipated. Plasma assisted oxidation of Si appears to stop Si etching after 2.5 nm of Si ratios) was removed – calculated using XPS peak intensities and equation (34).

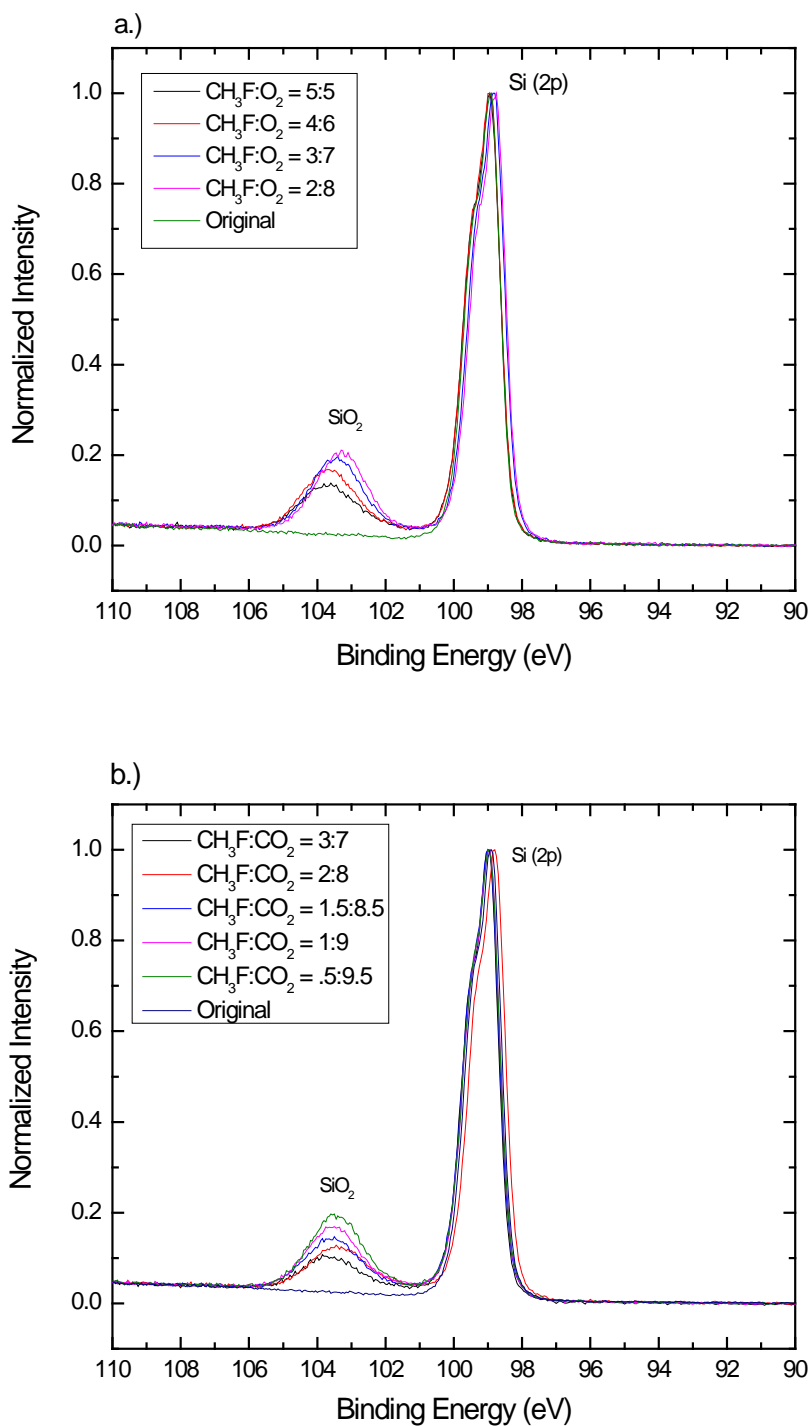
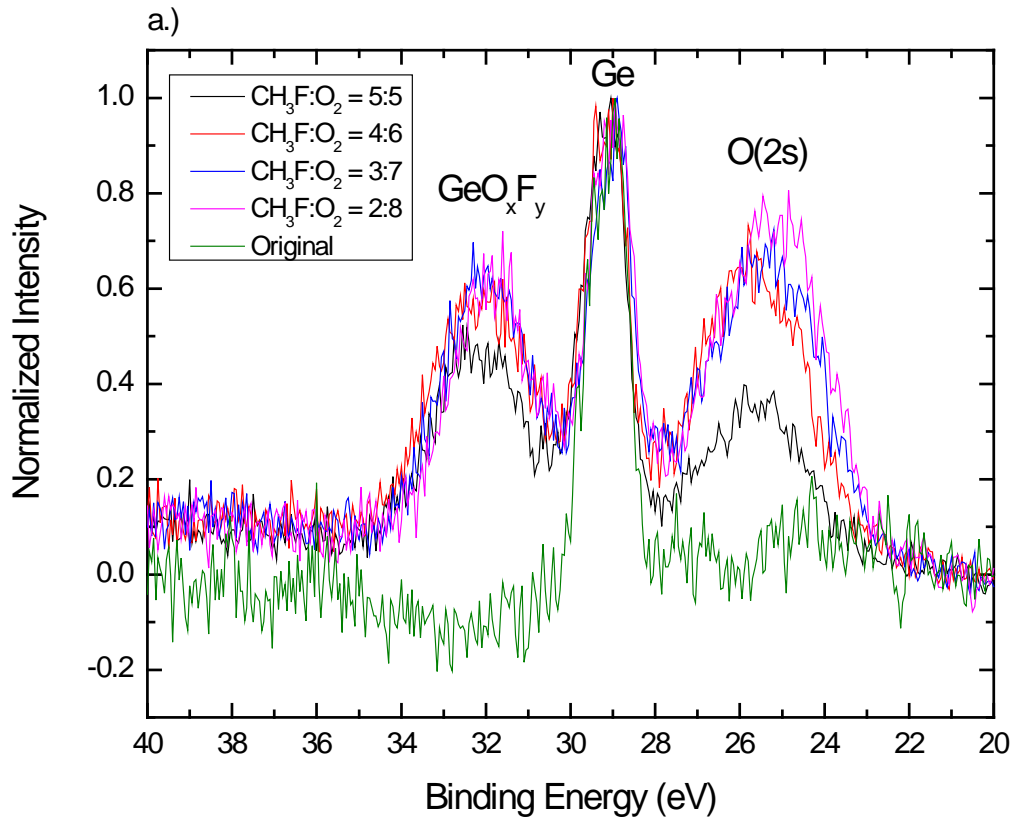


Fig. 29 XPS spectra of Si on Ge after exposing wafer to CH<sub>3</sub>F/O<sub>2</sub> (a.) and CH<sub>3</sub>F/CO<sub>2</sub> (b.) focused on Si (2p) region. Si (2p) peaks were normalized to unity at plasma conditions 300 W and 10 mTorr.

What was not anticipated was the appearance of an oxide/fluoride peak, labeled as  $\text{GeO}_x\text{F}_y$  in the Ge (3d) region, with exposure of the substrate to the plasma beam in conditions that result in very little of the Si layer being removed (figure 30 (a.) and (b.)). The magnitude of  $\text{GeO}_x\text{F}_y$ -to-Ge intensity ratio indicates that the oxyfluoride layer was several monolayers thick for both plasmas.



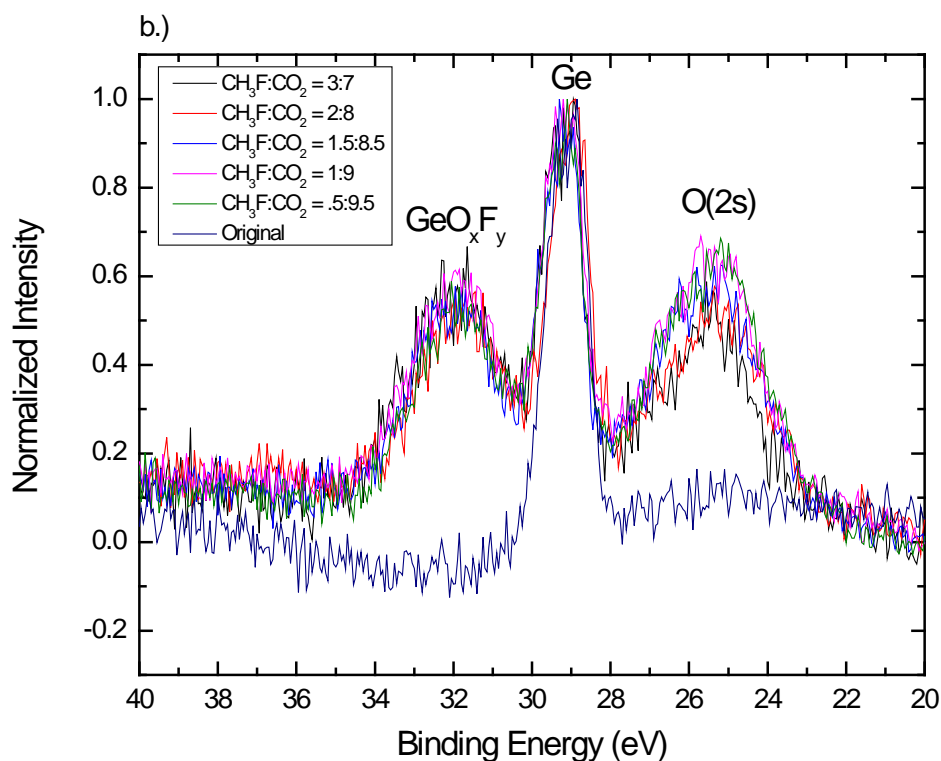


Fig. 30 XPS spectra of Si on Ge after exposing wafer to CH<sub>3</sub>F/O<sub>2</sub> (a.) and CH<sub>3</sub>F/CO<sub>2</sub> (b.) focused on Ge (3d) region. Ge (3d) peaks were normalized to unity at plasma conditions 300 W and 10 mTorr.

The only reasonable explanation was that F and/or O penetrate the 75 – 80 nm thick Si overlayer (100 nm the original thickness and 75-80 nm the “self-limiting” thickness found by XPS) and react with the underlying Ge. The intensity of the peak relative to Ge increases some between 50% and 60% O<sub>2</sub>, but then was constant between 60% and 80%, indicating that the Ge oxyfluoride layer reaches a saturated thickness *before* the surface Si oxyfluoride layer. It is also possible that the tensile stress in the Si layer (Si lattice constant is 0.543 nm and Ge is 0.568 nm)<sup>6,44</sup> could greatly aid the transport process.

The transport mechanism for F and/or O through the 10 nm thick Si film is not clear. Low energy heavy ions should penetrate no more than 1 nm, hence this does not seem to be a reasonable explanation. Fickian diffusion of F and O would be expected to be very slow at room temperature. Perhaps field assisted diffusion of F<sup>-</sup> or O<sup>-</sup> (i.e. Mott Cabrera mechanism) was occurring<sup>45-49</sup>.

#### **4.4 Deposition of Polymer Film on SiN<sub>x</sub>**

XPS analyses were done to measure in-situ polymer film thicknesses deposited on SiN<sub>x</sub>. Samples were, once again, turned away from the plasma source for 20s to reach steady-state CH<sub>3</sub>F/O<sub>2</sub> plasma conditions mentioned earlier. Deposition rates were calculated under the assumption that no polymer film deposited on the SiN<sub>x</sub> wafers during this 20s period. The substrate holder was then turned to face the plasma source for an additional 30s, 2 min, 3 min, and 3 min for 10% O<sub>2</sub>, 20 % O<sub>2</sub>, 30 % O<sub>2</sub>, and 40 % O<sub>2</sub> respectively. Their results are shown in figure 31. The film deposition rate sharply decreased as O<sub>2</sub> % addition approached the abrupt increase in O and F number density (polymer etchants) ~ 48% O<sub>2</sub>, shown in figure 16<sup>41</sup>. The maximum polymer deposition rate calculated was 37 Å/min.

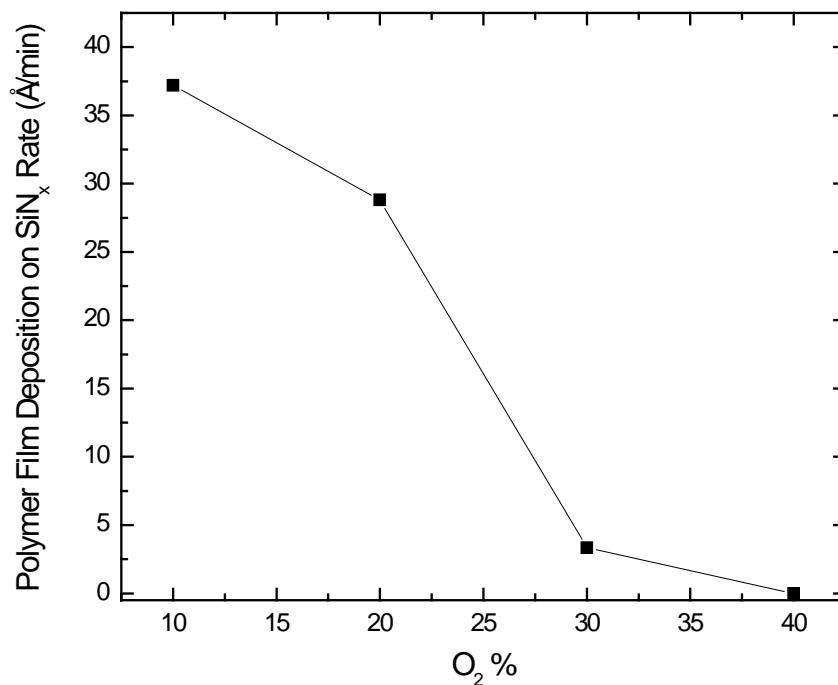
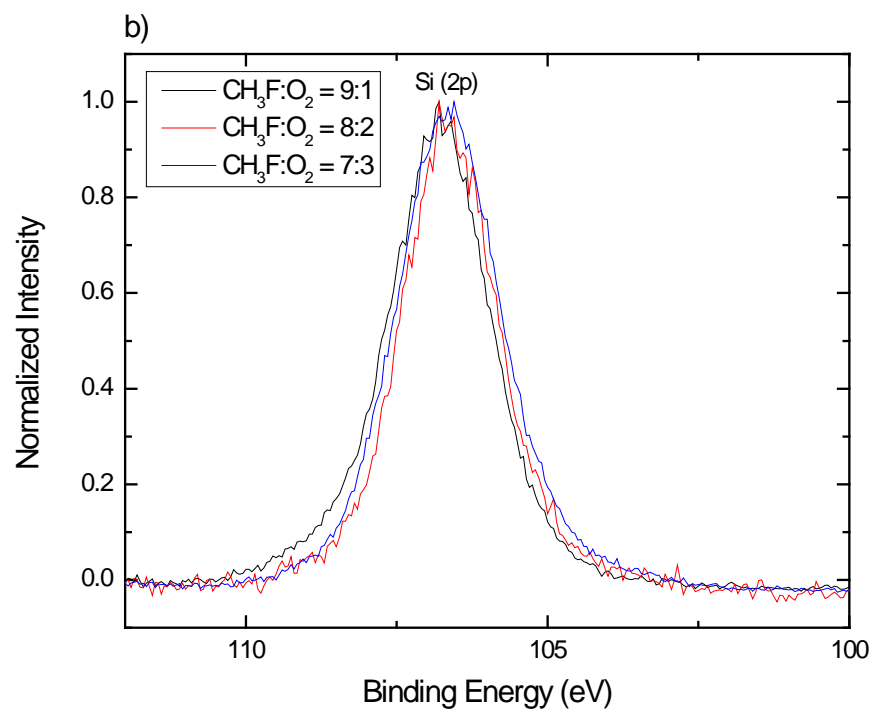
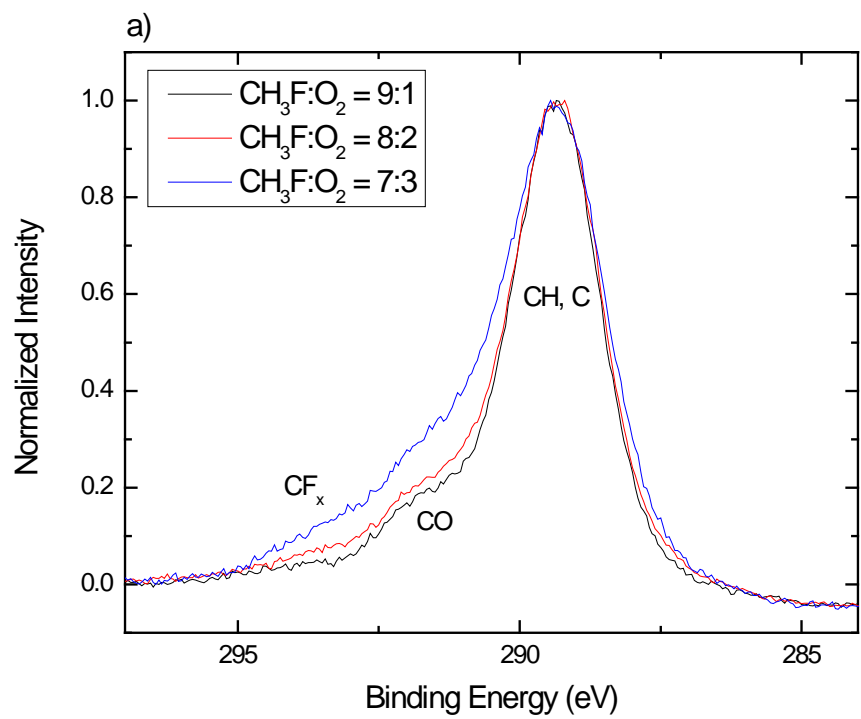
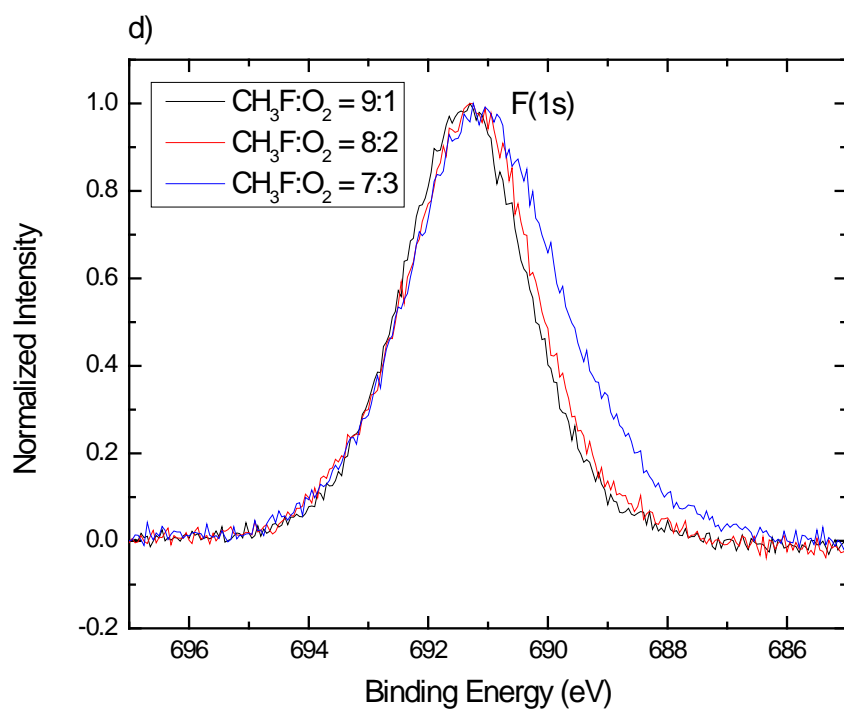
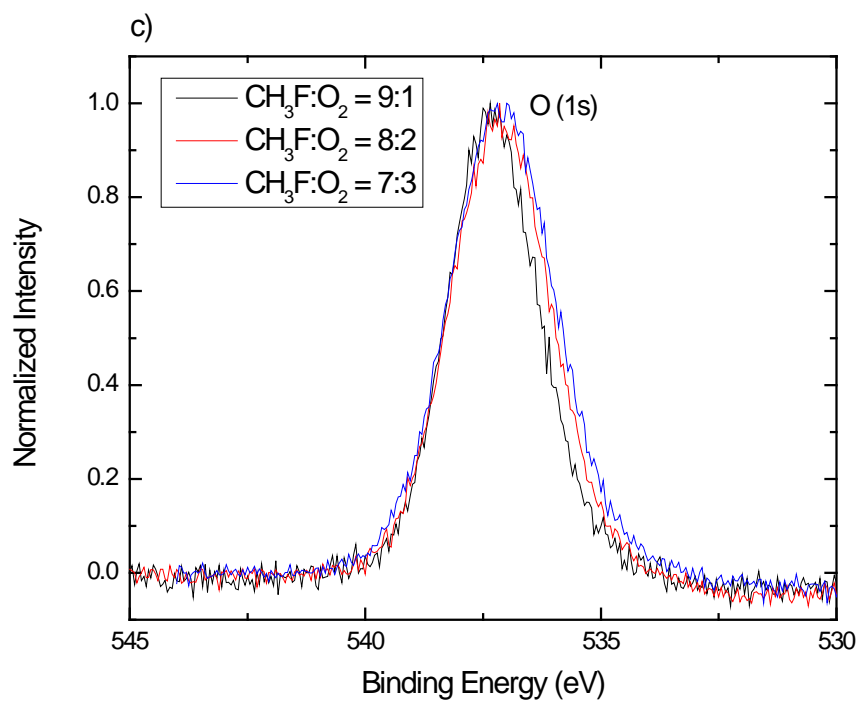


Fig. 31 Polymer film deposition on SiN<sub>x</sub> as function of O<sub>2</sub>% addition rates. CH<sub>3</sub>F/O<sub>2</sub> power and pressure was 300 W and 10 mTorr, respectively.

Figure 32 contains high resolution peaks normalized to unity after deposition of polymer onto SiN<sub>x</sub>. All peaks have shifted by about 4.83 eV, surface charging. The 286.4 eV (CO) and 288.8 eV (CF) peaks, which appears at 291.2 eV and 293.6 eV, increased relative to C (1s) peak at 284.3 eV (shifted to 289.4 eV) as O<sub>2</sub> % increased. This was similar a trend when compared with the polymer deposited on p-Si using CH<sub>3</sub>F/O<sub>2</sub> plasma, in figure 20 a). The O and CO number density results/behavior in figures 16 and 18 are also in good agreement with these findings. The Si(2p), O(1s), F(1s), and N(1s) detected at 106.7 eV, 537.1 eV, 691.1 eV, and 402.3 eV respectively, do not appear to differ from each-other as a function of % O<sub>2</sub> increase.





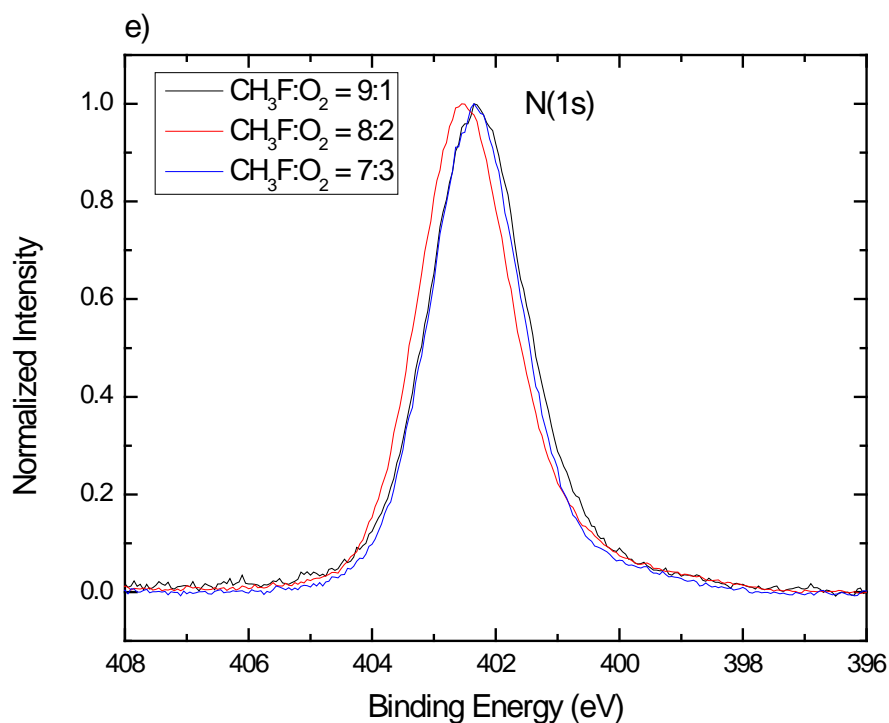


Fig. 32 XPS spectra of polymer film deposited on  $\text{SiN}_x$  comprising of a) C (1s), b) Si (2p), c) O (1s) d) F(1s), and e) N(1s) peaks.

#### 4.5 $\text{SiN}_x$ Etching with $\text{CH}_3\text{F}/\text{O}_2$ and $\text{CH}_3\text{F}/\text{CO}_2$ Plasmas

$\text{SiN}_x$  was etched using  $\text{CH}_3\text{F}/\text{O}_2$  and  $\text{CH}_3\text{F}/\text{CO}_2$  plasma at a power of 300 W, pressure of 10 mTorr, and flow rate of 10 sccm (no boundary bias). Spectroscopic ellipsometry was used to measure  $\text{SiN}_x$  thickness before and after plasma exposure. Figures 33 and 34 show the change in  $\text{SiN}_x$  thicknesses as a function of etch duration. After 20s of non-exposure, the substrate was turned towards the plasma beam for 1.5 min, 3 min, and 6 min at the polymer-free reactor walls composition of 80%  $\text{O}_2$  and 80%  $\text{CO}_2$ . A constant etch rate of 27 Å/min and 18 Å/min for 20%  $\text{CO}_2$  and 20%  $\text{O}_2$  was maintained independent of etch time. Figure 35 displays  $\text{SiN}_x$  etch rate as a function of %  $\text{O}_2$  and %  $\text{CO}_2$  addition. Faster etch rates are detected in  $\text{CH}_3\text{F}/\text{CO}_2$  than  $\text{CH}_3\text{F}/\text{O}_2$  over similar  $\text{CO}_2$  or  $\text{O}_2$  additions.

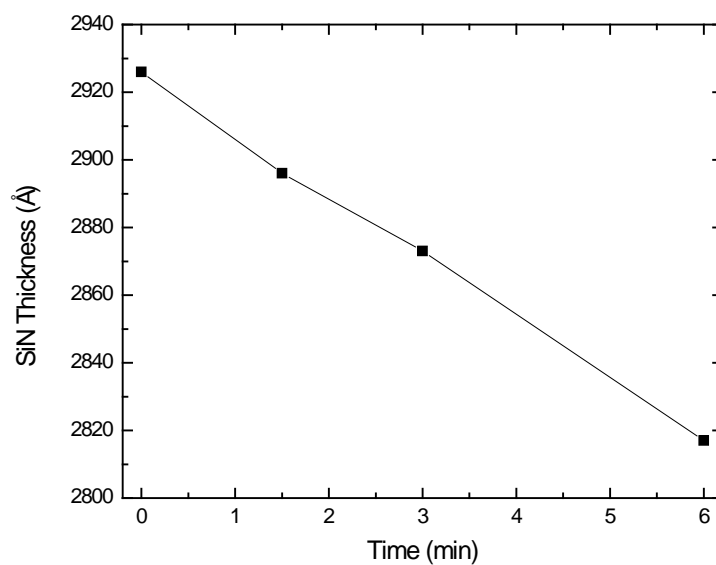


Fig. 33 SiN<sub>x</sub> thickness change was measured using an ellipsometry after exposing the substrate to CH<sub>3</sub>F 20% O<sub>2</sub> 80% plasma beam at a constant flow rate of 10 sccm. Plasma was maintained at 300 W and 10 mTorr without boundary bias.

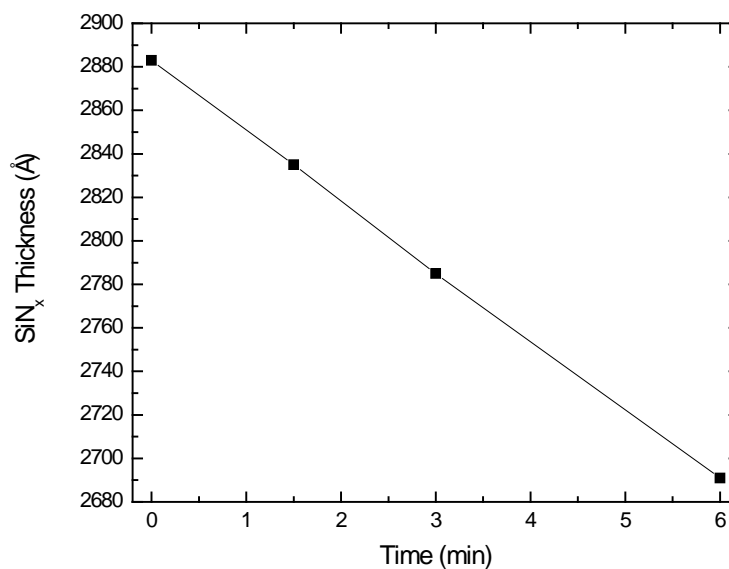


Fig. 34 SiN<sub>x</sub> thickness change was measured using an ellipsometry after exposing the substrate to CH<sub>3</sub>F 20% CO<sub>2</sub> 80% plasma beam at a constant flow rate of 10 sccm. Plasma was maintained at 300 W and 10 mTorr without boundary bias.

The reason for faster  $\text{SiN}_x$  etch rates in  $\text{CH}_3\text{F}/\text{CO}_2$  plasmas compared with  $\text{CH}_3\text{F}/\text{O}_2$  may possibly be explained by the reaction mechanisms (30) – (32), postulated by Chen et al.<sup>32</sup>. As discussed in chapter 3, Chen et al.<sup>32</sup> and Park et al.<sup>33</sup> propose the removal of N atoms is the major rate limiting steps in etching  $\text{SiN}_x$  using hydro-fluorocarbon plasmas. The Si/N ratio was decreased from 0.75, before  $\text{SiN}_x$  substrate was exposed to hydro-fluorocarbon plasma, to less than 0.5<sup>32,33</sup>. This would be consistent with  $\text{SiF}_x$  products being removed faster than N-containing products. The additional C atoms in  $\text{CH}_3\text{F}/\text{CO}_2$  plasma and the atomic C/Xe emission trend, in figure 16, gives evidence of the increased probability for forming  $\text{CN}^-$  involatile by-products during etching in the presence of the thin polymer layer over formed with 75% - 95%  $\text{O}_2$  and  $\text{CO}_2$  addition. OES measurements<sup>42</sup> and mass spectrometer spectra (figure 18) indicate atomic H are the abundant species in  $\text{CH}_3\text{F}/\text{CO}_2$  and  $\text{CH}_3\text{F}/\text{O}_2$  plasmas in the region of 75% - 95%  $\text{O}_2$  and  $\text{CO}_2$ . Therefore, it appears plausible that the formation of HCN form more readily in  $\text{CH}_3\text{F}/\text{CO}_2$  plasmas, compared with  $\text{CH}_3\text{F}/\text{O}_2$  plasmas.

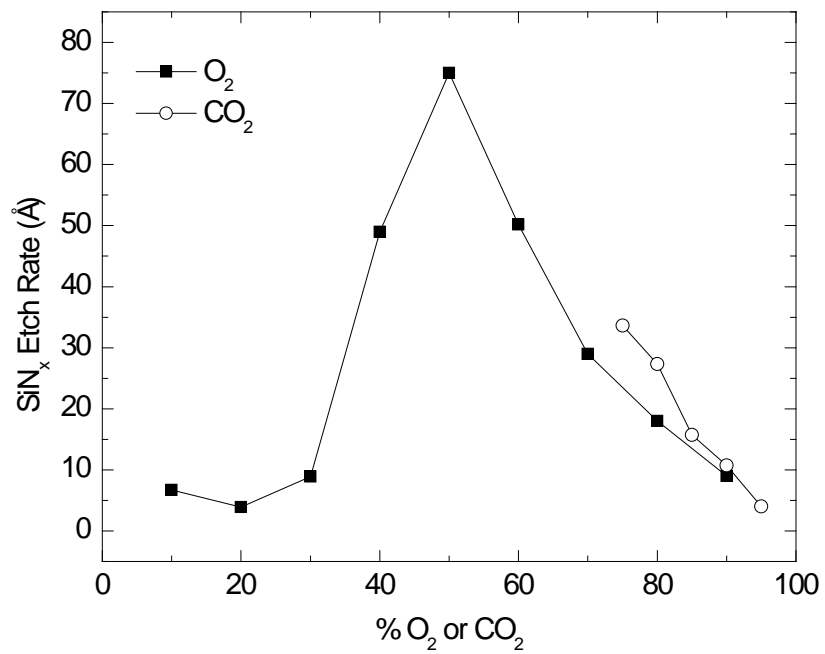


Fig. 35 SiN<sub>x</sub> etch rates measured using a spectroscopic ellipsometry as a function of O<sub>2</sub>% and CO<sub>2</sub> % addition. The plasma power was 300 W and pressure was 10 mTorr.

## Chapter 5 Summary and Conclusions

The use of silicon nitride films for integrated circuits has recently risen as feature sizes continue to decrease towards the atomic scale.  $\text{SiN}_x$  films are commonly used as hard mask material for various etching steps, for gate spacer formation, and as a final passivation/encapsulating layer<sup>5,30</sup>. It is vital to find ways to etch silicon nitride films with infinite/high selectivity over Si and  $\text{SiO}_2$  in nano-sized features.

Various experiment in  $\text{CH}_3\text{F}/\text{O}_2$  and  $\text{CH}_3\text{F}/\text{CO}_2$  inductively coupled plasmas were performed. The similarities/differences amongst the two hydro-fluorocarbon plasmas were initially investigated by optical emission spectroscopy and actinometry<sup>40-42</sup>. The etching of p-Si on Ge and  $\text{SiN}_x$  films using  $\text{CH}_3\text{F}/\text{O}_2$  and  $\text{CH}_3\text{F}/\text{CO}_2$  plasmas was carried out. The removal of Si on Ge stopped after the removal of 30 Å Si in both plasmas, likely due to the formation of a surface oxyfluoride layer. Most surprisingly, the underlying Ge layer becomes oxidized and/or fluorinated, possibly due to field assisted diffusion of  $\text{F}^-$  and  $\text{O}^-$  through the Si film.<sup>45-49</sup>  $\text{SiN}_x$  etch rates were faster in  $\text{CH}_3\text{F}/\text{CO}_2$  plasmas, compared with  $\text{CH}_3\text{F}/\text{O}_2$  plasmas in the region of 75%-95%  $\text{O}_2$  and  $\text{CO}_2$  addition, perhaps due to the increase in CN by products in the polymer film that then go on to react with impinging H atoms form volatile HCN. Polymer films were characterized by XPS and their deposition rates on p-Si and  $\text{SiN}_x$  were obtained and compared<sup>42</sup>. There were not many differences in polymer film composition in both plasmas. CO and  $\text{CF}_x$  peaks increased relative to C (1s) peak as %  $\text{O}_2$  and %  $\text{CO}_2$  increased on both  $\text{SiN}_x$  and p-Si. Larger film deposition rates on p-Si were found in  $\text{CH}_3\text{F}/\text{CO}_2$  plasmas, possibly due to the larger amount of solid C that will form at thermodynamic equilibrium in  $\text{CH}_3\text{F}/\text{CO}_2$  gas-phase mixtures.

## References

- (1) Schaller, R.R., *Spectrum, IEEE* , vol.34, no.6, pp.52,59, Jun 1997.
- (2) F. Faggin, M. E. Hoff, S. Mazor, and M. Shima, *IEEE Micro* 16, 10 (1996).
- (3) Bohr, M., & Mistry, K. (2011). “Intel’s Revolutionary 22 nm Transistor Technology”. Rob Willoner at Innovation.
- (4) V. M. Donnelly and A. Kornblit, *J. Vac. Sci. Technol. A* 31, 050825, 2013.
- (5) M. A. Lieberman and A. J. Lichtenberg, Principles of Plasma Discharges and Materials Processing, second ed. (John Wiley & Sons, Inc., 2005).
- (6) S.M. Sze, Physics of Semiconductor Devices. (John Wiley and Sons, Inc, New York, 1981).
- (7) Guillorn, M.; Chang, J.; Bryant, A.; Fuller, N.; Dokumaci, O.; Wang, X.; Newbury, J.; Babich, K.; Ott, J.; Haran, B.; Yu, R.; Lavoie, C.; Klaus, D.; Zhang, Y.; Sikorski, E.; Graham, W.; To, B.; Lofaro, M.; Tornello, J.; Koli, D.; Yang, B.; Pyzyna, A.; Neumeyer, D.; Khater, M.; Yagishita, A.; Kawasaki, H.; Haensch, W., *VLSI Technology, 2008 Symposium on* , vol., no., pp.12,13, 17-19 June 2008.
- (8) Kuo, Y. (1995). *Journal of The Electrochemical Society*, 142(1), 186-190.
- (9) Kastenmeier, B. E E; Matsuo, P. J.; Oehrlein, G.S., *Journal of Vacuum Science & Technology A: Vacuum, Surfaces, and Films* , vol.17, no.6, pp.3179,3184, Nov 1999.
- (10) Donnelly, V. M. and Flamm, D. L. and Dautremont-Smith, W. C. and Werder, D. J., *Journal of Applied Physics*, 55, 242-252 (1984),  
DOI:<http://dx.doi.org/10.1063/1.332872>.
- (11) C.J. Mogab, A. C. Adams, and D.L. Flamm *J. Appl. Phys.* **49**, 3796 (1978).

- (12) G. Smolinsky and D. L. Flamm, *J. Appl Phys.* 50, 4982 (1979).
- (13) Plumb, I. C., and K. R. Ryan. Plasma chemistry and plasma processing 6.3 (1986): 205-230.
- (14) d'Agostino, Riccardo and Cramarossa, Francesco and De Benedictis, Santolo and Ferraro, Giovanni. *Journal of Applied Physics*, 52, 1259-1265 (1981),  
DOI:<http://dx.doi.org/10.1063/1.329748>.
- (15) M. J. Vasile and F. A. Stevie, *Electrochem. Soc. Extend Abstr.* 81-2, 613 (1981).
- (16) M. J. Vasile, *Journal of Applied Physics*, 51, 2510 (1980).
- (17) R. Heinecke, *Solid State Electron.* 18, 1146 (1975).
- (18) R. Heinecke, *Solid State Electron.* 19, 1039 (1976).
- (19) Daniel L. Flamm, Vincent M. Donnelly, and John A. Mucha. *J. Appl. Phys.* 52, 3633 (1981).
- (20) C.I. M. Beenakker, J. H. J. van Dommelen, and J. Dieleman, *Electrochemical Society*, Vol. 80-1 St. Louis, May, 1980, p. 330; R. G. Frieser and C. J. Mogab, eds., *Electrochemical Society*, Vol. 81-1 New Jersey, 1981, p 302.
- (21) Daniel L. Flamm, and Vincent M. Donnelly, Plasma Chemistry and Plasma Processing Vol 1, Issue 4, pp 317-363 (Dec 1981).
- (22) E. P. G. T. van de Ven, P. A. Zijlstra, and R. Heinecke, *CVD Proj. RP7-78, Annual Report, Std. Telecom. Lab. Ltd.*, Harlow, Essex (1973).
- (23) R. Heinecke, *Solid State Electron* **18**, 1146 (1975).
- (24) R. Heinecke, *Solid State Electron* 19, 1039 (1976).
- (25) S. Matsuo, *J. Vac. Sci. Technol.* **17**, 587 (1980).
- (26) Y. Kurogi, M. Tajima, K. Mori, and K. Sugibuchi, *Electrochem. Soc. Extended*

*Abstr. 77-2* (1977).

- (27) S. Muramoto, T. Hosoya, and S. Matsu, *IEEE IEDM Tech. Digest*, p. 185 (1978).
- (28) S. Matsuo, *Jpn. J. Appl. Phys.* **17**, 235 (1978).
- (29) L. M. Ephrath, *J. Electrochem. Soc.* **126**, 1419 (1979) and H. Komiya, H. Toyoda, and H. Itakura, *Electrochem. Soc.*, Extended Abstr. **79-1** (1979).
- (30) O. Joubert; M. Darnon; G. Cunge; E. Pargon; D. Thibault; C. Petit-Etienne; L. Vallier; N. Posseme; P. Bodart; L. Azarnouche; R. Blanc; M. Haas; M. Brihoum; S. Banna; T. Lil, *SPIE* 8328, 83280D (2012).
- (31) Y. Iijima, Y. Ishikawa, C. Yang, M. Chang, and H. Okano, *Jpn. J. Appl. Phys.*, Part 1 **36**, 5498–5501 (1997).
- (32) L. L. Chen, L. D. Xu, D. X. Li, and B. Lin, *Microelectron. Eng.* **86**(11), 2354–2357 (2009).
- (33) C.K. Park, H.T. Kim, C.H. Lee, N.E. Lee, H. Mok *Microelectron. Eng.*, **85** (2008), p. 375.
- (34) B. E. E. Kastenmeier, P. J. Matsuo, and G. S. Oehrlein. *Journal of Vacuum Sciences Technologies. A* **17** (6), (1999).
- (35) T.E.F.M. Standaert, C. Hedlund, E.A. Joseph, G.S. Oehrlein, T.J. Dalton, *J. Vac. Sci. Technol. A* **22** (2004) 53.
- (36) N.R. Rueger, J.J. Beulens, M. Schaepkens, M.F. Doemling, J.M. Mirza, T.E.F.M. Standaert, G.S. Oehrlein, *J. Vac. Sci. Technol. A* **15** (1997) 1881.
- (37) Wang, C. and Donnelly, V. M., *Journal of Vacuum Science & Technology B*, **23**, 547-553 (2005), DOI:<http://dx.doi.org/10.1116/1.1875292>.
- (38) Pelhos, K. and Donnelly, V. M. and Kornblit, A. and Green, M. L. and Van

- Dover, R. B. and Manchanda, L. and Hu, Y. and Morris, M. and Bower, E.,  
*Journal of Vacuum Science & Technology A*, 19, 1361-1366 (2001),  
 DOI:<http://dx.doi.org/10.1116/1.1349721>.
- (39) M. Matsui, T. Tatsumi, M. Sekine, *J. Vac. Sci. Technol. A* 19 (2001).
- (40) Karakas, Erdinc; Donnelly, Vincent M.; Economou, Demetre J., *Applied Physics Letters*, vol.102, no.3, pp.034107,034107-4, Jan 2013 doi: 10.1063/1.4789435.
- (41) Erdinc Karakas, Vincent M. Donnelly, and Demetre J. Economou., *J. Applied Physics*, vol 113, 000000 (2013).
- (42) Qiaowei Lou, Sanbir Kaler, Vincent M. Donnelly, and Demetre J. Economou. To be published.
- (43) Seah, M. P., and W. A. Dench. *Surface and Interface Analysis* 1.1 (1979): 2-11.
- (44) S. Wolf, R. Tauber., Silicon Processing for the VLSI Era. (Lattice Press, Sunset Beach, California, 1986.)
- (45) Cabrera N and Mott N F 1949 *Rep. Prog. Phys.* 12 163-84.
- (46) K. Koshino, J. Matsuo, and M. Nakamura, *Jpn. J. Appl. Phys.*, Part 1 32, 3063 (1993).
- (47) T. Morimoto, *Jpn. J. Appl. Phys.*, Part 1 32, 1253 (1993).
- (48) K. Kim, M. H. An, Y. G. Shin, M. S. Suh, C. J. Youn, Y. H. Lee, K. B. Lee, and H. J. Lee, *J. Vac. Sci. Technol. B* 14, 2667 (1996).
- (49) A. Dolique and A. H. Reader, *J. Non-Cryst. Solids* 187, 29 (1995).

